Optimal quantum gates for Rydberg atoms quantum computer

Master Degree in Physics of Data

Candidate:

Alice Pagano

Thesis supervisor:	Prof. Simone Montangero
Thesis co-supervisor:	Prof. Hans Peter Büchler
Day of the Final Dissertation:	15 September 2021

Dipartimento di Fisica e Astronomia "Galileo Galilei"

Università degli studi di Padova

A.A. 2020/21

Abstract

Arrays of identical neutral atoms trapped in optical tweezers are a promising candidate for use in quantum computing. These platforms are highly scalable to large numbers of qubits and neutral atoms boost several attractive features as long coherence times and the possibility to be entangled via strong dipole-dipole interactions by driving them to highly excited Rydberg states. The Thesis work is developed inside the framework of the QRydDemo project, whose aim in the next few years is to realize a neutral atom quantum processor with several hundred qubits. The smallest building blocks for the quantum computer are one and two-qubit gates: to entangle two atoms in the quantum register, a controlled-phase (CZ) gate will be implemented by shining fine-tuned laser pulses onto them. In this work, after giving a theoretical description of the Hamiltonian of two neutral atoms in the quantum register, a numerical simulation of this system is exploited to reproduce the behavior of the two-qubit CZ gate. Realistic effects are taken into account as finite temperature, imperfect Rydberg blockade, or decay out of the Rydberg state. A protocol with constant pulses is analyzed and its optimal parameters are found through classical optimizers. Then, time-dependent pulses are introduced and the optimal pulses are found through the optimal control algorithm dCRAB in an open-loop optimization. For the experimental realization of the gate, this analysis is of pivotal importance to know in which aspect more effort has to be put to maximize the experimental precision of the operation and thus improving the performance of the whole device.

Contents

Introduction

In 1982 Richard Feynman introduced for the first time the idea of quantum computing [1]: he suggested that a quantum mechanical device, a *quantum computer*, had the potential to simulate more efficiently than a classical computer the probabilistic quantum nature of the physical world. Quantum computation promises advantages on a large variety of fields from condensed-matter problems [2] and high-energy physics [3] to industrial applications [4]. Although the *quantum supremacy* had not been demonstrated yet, in the last years there has been remarkable experimental and theoretical progress towards making this idea a reality [5–7]. Inspired by classical computing, one way to define a quantum computation algorithm is through a *quantum circuit* that describes the computation in terms of a network of quantum logic gates [8]. A quantum circuit manipulates the information stored in a set of two-level systems called *qubits* by exploiting purely quantum phenomenon as entanglement. From an experimental point of view, generating and managing qubits is a challenge since quantum devices are extremely susceptible to noise sources [9]. Over the past few decades, various quantum devices have been developed, among which, the more established ones are *superconducting loops* [10], *trapped ions* [11], and *neutral atoms* [12]; for each of these different platforms, an effective two-level system is implemented to realize the qubit and the gates are operations acting on them. Considerable efforts are dedicated to improving all these platforms, each with its strengths and weaknesses, and the race to develop a fully functional quantum computer is currently ongoing.

Arrays of identical neutral atoms trapped in optical tweezers, which are the study of this Thesis, boost several attractive features, one for all the high scalability to large numbers of qubits. Indeed, many atoms can be packed close together since neutral atoms separated by more than a few Angstroms interact very weakly. Moreover, neutral atoms present long decoherence times and they can be individually and accurately controlled by using electromagnetic fields [13]. However, to implement entangling operations strong interactions among qubits are required. Given the weak interaction between neutral atoms, a solution is to temporarily excite them to Rydberg states. The study of Rydberg atoms began in the early stage of atomic physics at the end of the 1800s, when the Swedish physicist Johannes Rydberg introduced a formula describing the relation between the wavelengths in spectral

lines of alkali metals. With the birth of tunable lasers in the 1970s, the extreme sensitivity of Rydberg atoms to microwave radiation made them ideal to study atom-light interaction. At the end of the 1990s, it was proposed for the first time to exploit the strong interaction between neutral atoms excited to Rydberg states to realize entangling quantum gates [14, 15]. This is possible thanks to the *Rydberg blockade* effect which prevents the simultaneous Rydberg excitation of two nearby atoms. However, only recently the progress in the manipulation of individual Rydberg atoms has allowed the physical implementation of high-fidelity gates between neutral atoms [16]. In 2019, it has been shown how to implement a controlled-phase gate with a Bell-state fidelity greater than 97.4% with Rubidium-87 atoms [17]. In 2020, it has been demonstrated a Bell-state fidelity greater than 99.1% switching to a Strontium-88 platform [13]. These very exciting results show how Rydberg gates can achieve very high fidelity. They are also fast with a typical gate time of the order of $100\,\text{ns}$. However, the single-qubit coherence time is limited to $\sim 10\,\mu\text{s}$ so far.

This Thesis has been developed in the framework of the QRydDemo project, which in the next few years aims to realize a neutral atom quantum computer demonstrator with several hundred qubits. The main aim of the project is to improve the coherence time up to three orders of magnitude solving the technical problems that up to now are limiting applications as quantum computers. This improvement would give more flexibility for the implementation of new type of algorithms and thus exploring new scenarios. The physical hardware is based on individually controlled Strontium-88 atoms trapped in a two-dimensional array by using optical tweezers. The main idea is to encode the qubit in two very long-lived states of a metastable triplet state. The coherence time can be considerably increased by setting the frequency of the tweezers to a specific value, that we call *magic wavelength*, which allows one to reach an optimal, or magic, trapping condition. In this setup, rotations around the z-axis by an arbitrary angle are implemented via AC Stark shift using a Raman laser. Rotations around the x-axis by an arbitrary angle are realized by coupling the two-qubit states via the Raman transition. However, in a quantum platform, it is not enough to implement only single-qubit operations. To entangle two atoms in the QRydDemo platform, a controlled-phase (CZ) gate will be implemented by driving atoms to highly excited Rydberg states and thus exploiting the Rydberg blockade effect.

In this work, the different contributions to the total system Hamiltonian of two atoms in the quantum register are analyzed such as the trapping in the optical tweezer, the atom-light interaction, and the Rydberg atoms interaction. This system is simulated by Sebastian Weber, within the QRydDemo project, in order to reproduce the behavior of a two-qubit CZ gate. The simulation takes into account realistic effects as finite temperature, imperfect Rydberg blockade, or decay out of the Rydberg state. Realistic parameters for the QRydDemo device are considered. The aim of our analysis is to explore which kind of protocol for the gate implementation works best on this platform and to benchmark theoretically

the maximum gate fidelity achievable. Firstly, a protocol developed in Ref. [17] is analyzed. It consists of just two global laser pulses with Rabi frequency Ω and with the laser phase of the second pulse shifted by ξ. The two pulses have the same length τ and a constant detuning Δ which couples the excited state $|1\rangle$ to the Rydberg state $|r\rangle$ and they drive nearest neighbour atoms to the Rydberg blockade regime. The optimal time duration τ, detuning Δ, and phase shift ξ which maximize the gate fidelity are found through classical optimizers. Then, a time-dependent detuning $\Delta(t)$ is introduced to investigate if this can lead to an improved fidelity. In this case, the optimal $\Delta(t)$ pulse is found through the optimal control algorithm dCRAB in an open-loop optimization [18]. The analysis is also performed by introducing a realistic finite bandwidth for Ω, Δ and ξ. After that, a protocol consisting of a global laser pulse of duration 2τ with Rabi frequency Ω, a zero phase and a time-dependent detuning with a triangular shape is analyzed. Also in this case, the optimal parameters are first found through classical optimizers and then the optimal control algorithm is applied to investigate if there could be a gain in fidelity. Finally, we show that a protocol with a time-dependent phase and constant detuning is equivalent to the one with a zero phase and a time-dependent, within a unitary transformation.

This Thesis is structured as follows:

→ In Chapter 1, the fundamental concepts of quantum computation are shortly reviewed to provide a first general insight into quantum computer development from a generic theoretical perspective. We start with the notion of the qubit and we discuss how pure states are represented in a computational basis. Then, we introduce the model of quantum circuits and we show the representation of the most popular quantum gates. After that, we briefly discuss the density matrix formalism to represent the most general mixed states and the time evolution of closed and open quantum systems are shortly reviewed. The operator-sum representation is also introduced to include selected open system effects to the previously ideal quantum processes. In the end, we discuss how to represent quantum states at finite temperature.

→ In Chapter 2, we provide a general insight into the theoretical basis of neutral atoms quantum devices. First of all, the physical description and the main properties of independent Rydberg atoms are reviewed. Then, we discuss the interaction of Rydberg atoms via the electric dipole-dipole operator and we describe the main mechanism of Rydberg blockade. Afterward, we explain how to create/assemble arrays of neutral atoms: they are trapped in optical tweezers which can be modeled as harmonic oscillators from a theoretical perspective. To understand how neutral atoms can be excited, the foundation of atom-light interaction is also reviewed.

→ In Chapter 3, the optimal control algorithm dCRAB is reviewed as well as its implementation on the open source quantum optimal control suite.

→ Chapter 4 gives a brief overview of the experimental apparatus at the basis of a neutral atom quantum processor by reference to the QRydDemo processor. The main steps of one computation cycle, namely register loading, quantum processing and register readout, are analyzed. Then, the total system Hamiltonian of two neutral atoms in the register is described in detail. It is implemented numerically by the members of the QRydDemo project to perform a simulation of the system to reproduce the behavior of a two-qubit CZ gate. The simulation takes into account realistic effects, such as the trapping in the optical tweezer at a finite temperature, the decay out of the Rydberg state $|r\rangle$ or an imperfect blockade regime.

→ In Chapter 5, we show the main results of the numerical simulation of the two-qubit CZ gate. As already mentioned, we start from the proposal shown in Ref. [17] and we theoretically benchmark this protocol for the QRydDemo platform. The optimal control algorithm dCRAB is used to improve the gate fidelity. After that, a new proposal with a triangular detuning shape is discussed. Finally, we show that these two protocols are related by a unitary transformation.

Part I

Concepts for quantum computation and neutral atoms

Chapter 1

Basics of Quantum Computing

"Never underestimate the joy people derive from hearing something they already know."

— Enrico Fermi

In this Chapter, the fundamental concepts of quantum computation are reviewed. In Sec. 1.1, we introduce the general concept of a *qubit* and discuss its representation on the so-called *Bloch sphere*. In Sec. 1.2 we review the *quantum circuit* model for performing quantum computation and the definition of *quantum gates* is given. In Sec. 1.3 we introduce the density matrix formalism, a useful tool to describe systems interacting with an external environment. Then, in Sec. 1.5 we discuss different kinds of measures to compare noisy and ideal quantum processes. Finally, in Sec. 1.6 we review quantum systems at a finite temperature and a method to simulate them based on sampling *minimally entangled typical thermal states*.

1.1 Quantum bit

A quantum bit (or *qubit*) is the quantum version of the classic binary bit. It is a two-level quantum system where the two basis qubit states are denoted as $|0\rangle$ and $|1\rangle$ [8]. Generally, a pure qubit state is a unit vector in a two-dimensional Hilbert space and can be written as a linear combination, or *superposition*, of the basis states:

$$|\psi\rangle = \alpha\,|0\rangle + \beta\,|1\rangle\,, \tag{1.1}$$

where $\alpha, \beta \in \mathbb{C}$ are probability amplitudes with the constraint $|\alpha|^2 + |\beta|^2 = 1$.

1.1.1 Bloch sphere representation

Any possible quantum state for a single qubit can be geometrically visualized. Indeed, with a suitable change of coordinates and exploiting the undetectability of global phases in quantum mechanics, it is possible to rewrite the probability amplitudes α and β as follows:

$$|\psi\rangle = \cos\frac{\theta}{2}|0\rangle + e^{i\varphi}\sin\frac{\theta}{2}|1\rangle\,, \tag{1.2}$$

where $0 \leq \theta \leq \pi$ and $0 \leq \varphi < 2\pi$. The angles θ and φ define a point on a three-dimensional unitary sphere, called *Bloch sphere* illustrated in Fig. 1.1. The state $|0\rangle$ occupies the north pole and the state $|1\rangle$ the south pole, and any point at the surface of the sphere is associated with another unique qubit state, being a coherent superposition of $|0\rangle$ and $|1\rangle$.

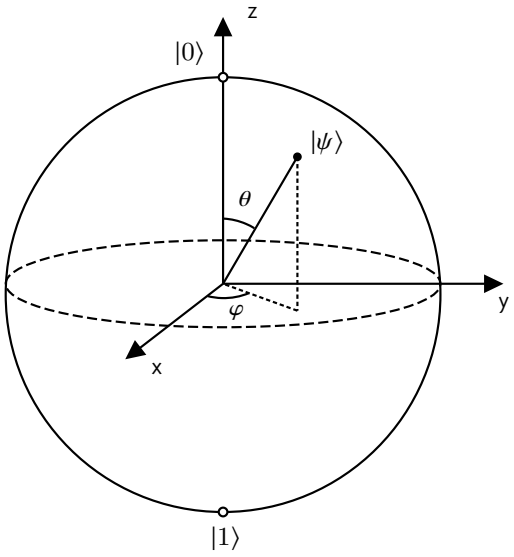

FIGURE 1.1 • Qubit state visualization on the Bloch sphere. The basis state $|0\rangle$ is represented by the unit vector $\hat{z}$ while the basis state $|1\rangle$ by $-\hat{z}$. Any point at the surface of the sphere is associated with a qubit state given by $|\psi\rangle = \cos\frac{\theta}{2}|0\rangle + e^{i\varphi}\sin\frac{\theta}{2}|1\rangle$.

1.1.2 Multiple qubits and entanglement

The states of the quantum system of N distinguishable qubits live in a Hilbert space of dimension 2^N given by the tensor product of the Hilbert spaces $\mathcal{H}_i$ of the single qubits:

$$\mathcal{H} = \mathcal{H}_1 \otimes \cdots \otimes \mathcal{H}_N. \tag{1.3}$$

Given the state $|j\rangle_i$ of the i-th qubit, a generic state $|\psi\rangle \in \mathcal{H}$ can be written as:

$$|\psi\rangle = \sum_{j_1 \dots j_N \in \{0,1\}^N} c_{j_1 \dots j_N} |j\rangle_1 \dots |j\rangle_N \tag{1.4}$$

with the constraint $\sum_{j_1 \dots j_N \in \{0,1\}^N} |c_{j_1 \dots j_N}|^2 = 1$.

The power of quantum computation relies on purely quantum phenomena as *entanglement*, that entails an intrinsic correlation between the constituents of a quantum system. Given an N-qubit system, a quantum state is said to be entangled if it cannot be factorized as a tensor product of states of its local constituents. The simplest example of entangled states are the *Bell states* for a two-qubit system:

$$\left|\Phi^+\right\rangle = \frac{1}{\sqrt{2}}(|00\rangle + |11\rangle) \tag{1.5a}$$

$$|\Phi^-\rangle = \frac{1}{\sqrt{2}}(|00\rangle - |11\rangle) \tag{1.5b}$$

$$\left|\psi^+\right\rangle = \frac{1}{\sqrt{2}}(|01\rangle + |10\rangle) \tag{1.5c}$$

$$|\psi^-\rangle = \frac{1}{\sqrt{2}}(|01\rangle - |10\rangle). \tag{1.5d}$$

1.2 Quantum circuit

Quantum computation consists of acting on a qubit register by means of a quantum algorithm. It is useful to use the *quantum circuit* model in which quantum algorithms are decomposed into a sequence of quantum gates performed on one or more qubits. In general, an N-qubit *quantum gate* is an operation that is applied on N qubits changing their quantum state. It can be represented by a unitary matrix generically indicated as $\hat{U}$ of dimension $2^N \times 2^N$.

As unitary transformations, any single-qubit gate corresponds to a rotation of the state vector onto the Bloch sphere. In this respect, they can always be written as combinations of the Pauli matrices $\hat{\sigma}_x$, $\hat{\sigma}_y$ and $\hat{\sigma}_z$. A single-qubit gate of paramount importance is the *Hadamard gate*, defined as:

$$\hat{\mathrm{H}} = \frac{1}{\sqrt{2}} \begin{pmatrix} 1 & 1 \\ 1 & -1 \end{pmatrix} = \frac{(\hat{\sigma}_x + \hat{\sigma}_z)}{\sqrt{2}}. \tag{1.6}$$

It maps the basis state $|0\rangle$ to $\frac{(|0\rangle+|1\rangle)}{\sqrt{2}}$ and $|1\rangle$ to $\frac{(|0\rangle-|1\rangle)}{\sqrt{2}}$, thus creating an equal superposition of the two basis states. In the Bloch sphere, it corresponds to a π rotation around the $(x + z)$ axis.

Two-qubit gates are unitary transformations described by 4×4 matrices that transform one two-qubit state into another. They are the most basic but crucial resource allowing the generation of entanglement between qubits. An important two-qubit gate is the *controlled-phase* (or *CZ*) gate:

$$\hat{C}_Z = \begin{pmatrix} 1 & 0 & 0 & 0 \\ 0 & -1 & 0 & 0 \\ 0 & 0 & -1 & 0 \\ 0 & 0 & 0 & -1 \end{pmatrix}. \tag{1.7}$$

It is an example of a controlled unitary operator gate where the two qubits in input are designated as the *target* and *control* respectively. The gate has no effect on the control qubit but performs a unitary operation on the target qubit conditionally on the state of the control qubit.

Together with arbitrary single-qubit gates, the entangling operation forms a *universal* quantum computing gate set: they are sufficient for the realization of any quantum algorithm. For instance, the two-qubit CZ gate can be combined with a set of generators for single-qubit gates to form a universal set of gates [19].

A quantum circuit is usually concluded with a *measurement* of one or more qubits. It is an irreversible operation that destroys quantum information and converts it into a classical one.

1.2.1 Creating Bell states

To provide an example of a simple quantum circuit, let us show the procedure [20] to prepare the Bell state of Eq. (1.5a) using only the Hadamard and the controlled-phase gates previously described:

1 start with the separable state $|11\rangle$;

2 apply the Hadamard gate to both qubits:

$$|\text{in}\rangle = \hat{H}_1 \hat{H}_2 |11\rangle = \frac{1}{2}(|00\rangle - |01\rangle - |10\rangle + |11\rangle); \tag{1.8}$$

3 apply the $\hat{C}_Z$ gate to $|\text{in}\rangle$;

4 then, apply a Hadamard gate on qubit 2 to obtain the Bell state $|\Phi^+\rangle$.

1.3 Density matrix formalism

Pure states, described by state vectors $|\psi\rangle$ on Hilbert space as in Subsec. 1.1.2, are an idealized description. They cannot characterize statistical (incoherent) mixtures, which often occur in the experiment due to interaction with the environment. To describe this situation in more abstract terms, the information regarding the system is not complete and the system's state is associated with an ensemble of pure states: a *mixed* state. A formulation that can encode all the (accessible) information about a quantum mechanical system and can represent both pure states and mixed states is the *density matrix representation*.

1.3.1 General properties

Each quantum state can be represented by an operator ρ, called *density matrix*, with the following properties:

I $\rho^\dagger = \rho$ *hermiticity*

II $\mathrm{Tr}\,\rho = 1$ *normalization*

III $\forall\,|u\rangle : \langle u|\,\rho\,|u\rangle \geq 0$ *positivity*

If we fix an arbitrary basis $\{|i\rangle\}_{i=1}^N$ of the Hilbert space the density matrix in this basis is written as $\rho = \sum_{i,j=1}^N \rho_{i,j}\,|i\rangle\langle j|$, or

$$\rho = \begin{pmatrix} \rho_{00} & \rho_{01} & \cdots & \rho_{0N} \\ \rho_{10} & \rho_{11} & \cdots & \rho_{1N} \\ \vdots & \vdots & \ddots & \vdots \\ \rho_{N0} & \rho_{1N} & \cdots & \rho_{NN} \end{pmatrix}, \tag{1.9}$$

where the diagonal elements are called *populations* ($\rho_{ii} \in \mathbb{R}_0^+$ and $\sum_i \rho_{ii} = 1$), while the off-diagonal elements are called *coherences* ($\rho_{ij} \in \mathbb{C}$ and $\rho_{ij} = \rho_{ji}^*$).

The expectation value of an observable $\hat{A}$ in a state, represented by a density matrix ρ, is given by

$$\langle \hat{A} \rangle_\rho = \mathrm{Tr}\left(\rho \hat{A}\right). \tag{1.10}$$

1.3.2 Pure and mixed states

If the system can be fully described by a state vector $|\psi\rangle$, the density matrix ρ for the *pure* state $|\psi\rangle$ is given by

$$\rho = |\psi\rangle\langle\psi| . \tag{1.11}$$

Since the density matrix for a pure state is a projector, it is an *idempotent*: $\rho^2 = \rho$. By combining this property and $\mathrm{Tr}\,\rho = 1$, a pure state is characterized by

$$\mathrm{Tr}\,\rho^2 = 1. \tag{1.12}$$

Most generally, a quantum system can be in one state of a set $\{|\psi_i\rangle\}$ with probabilities p_i. Therefore, our knowledge of the system is given by an ensemble of pure states described by the set $\{|\psi_i\rangle\,, p_i\}$. If more than one p_i is different from zero the state is not pure anymore, and it is called a *mixed* state. The latter can be written as a convex sum of pure state density matrices

$$\rho = \sum_i p_i\, |\psi_i\rangle\langle\psi_i| , \tag{1.13}$$

where $\sum_i p_i = 1$ and with the property $\mathrm{Tr}\,\rho^2 < 1$.

1.3.3 Reduced density matrix

Consider a quantum system composed of subsystems A and B with Hilbert space $\mathcal{H} = \mathcal{H}_A \otimes \mathcal{H}_B$ and fully described by the density matrix ρ_{AB}. The *reduced density matrix* of subsystem A is then given by:

$$\rho_A = \mathrm{Tr}_B(\rho_{AB}), \tag{1.14}$$

where Tr_B is the *partial trace* operation over the system B. Let $\{|a_i\rangle\}$ be a basis of $\mathcal{H}_A$ and $\{|b_i\rangle\}$ of $\mathcal{H}_B$ the partial trace function, taken over subsystem B, is defined [21] as

$$\mathrm{Tr}_B(\rho_{AB}) = \mathrm{Tr}_B\left[\sum_{ijkl} |a_i\rangle\langle a_j| \otimes |b_k\rangle\langle b_l|\right] = \sum_{ij} |a_i\rangle\langle a_j| \,\mathrm{Tr}\left[\sum_{kl} |b_k\rangle\langle b_l|\right]. \tag{1.15}$$

1.4 Time evolution

1.4.1 Closed quantum systems

The dynamics of a closed pure quantum system is governed by the Schrödinger equation

$$i\hbar\frac{\partial\,|\psi\rangle}{\partial t} = \hat{\mathrm{H}}\,|\psi\rangle\,, \tag{1.16}$$

where $|\psi\rangle$ is the wavefunction, $\hat{\mathrm{H}}$ the Hamiltonian of the system and $\hbar$ the Planck's constant. The formal solution is $|\psi(t)\rangle = \hat{U}(t,t_0)\,|\psi(t_0)\rangle$, where the unitary operator $\hat{U}$, also called *propagator*, is the solution of the equation

$$i\hbar\frac{\partial\hat{U}}{\partial t} = \hat{\mathrm{H}}\hat{U}(t,t_0). \tag{1.17}$$

If the Hamiltonian is time-independent, the propagator has the form $\hat{U}(t,t_0) = e^{-\frac{i}{\hbar}\hat{\mathrm{H}}(t-t_0)}$.

The equivalent of the Schrödinger equation in the density matrix formalism is the *Liouville-von Neumann* equation

$$i\hbar\frac{\partial\rho}{\partial t} = [\hat{\mathrm{H}},\rho]. \tag{1.18}$$

The solution of the von Neumann equation is:

$$\rho(t) = \hat{U}(t,t_0)\rho(t_0)\hat{U}^{\dagger}(t,t_0). \tag{1.19}$$

In the next subsection, we present how to evolve the density matrix as an open system instead of a closed system.

1.4.2 Open quantum systems

While the evolution of the state vector in a closed quantum system is deterministic, open quantum systems are stochastic in nature. As we have seen, the state of an open quantum system is therefore described in terms of ensemble averaged states with the density matrix ρ. The standard approach to derive the equations of motion for a system interacting with its environment is to expand the system to include the environment. The combined quantum system encoded in ρ_{tot} is then closed, and its evolution is governed by the von Neumann equation Eq. (1.18) with Hamiltonian

$$\hat{\mathrm{H}}_{\mathrm{tot}} = \hat{\mathrm{H}}_{\mathrm{sys}}\otimes\mathbb{1}_{\mathrm{env}} + \mathbb{1}_{\mathrm{sys}}\otimes\hat{\mathrm{H}}_{\mathrm{env}} + \hat{\mathrm{H}}_{\mathrm{int}}, \tag{1.20}$$

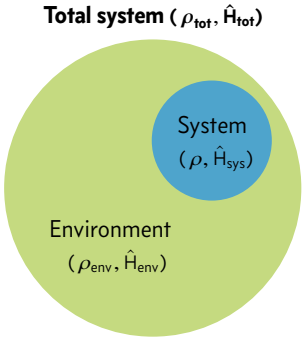

FIGURE 1.2 • An open quantum system with the density matrix ρ and Hamiltonian $\hat{H}_{sys}$ and the environment represented by ρ_{env} and $\hat{H}_{env}$ form a closed quantum system, i.e., the density matrix ρ_{tot} and the Hamiltonian $\hat{H}_{tot}$. The total Hamiltonian $\hat{H}_{tot}$ contains the contributions of the system, the environment and the interaction between them.

which includes the original system Hamiltonian $\hat{H}_{sys}$, the Hamiltonian for the environment $\hat{H}_{env}$, and a term representing the interaction between the system and its environment $\hat{H}_{int}$. Since we are only interested in the dynamics of the system, we can at this point perform a partial trace over the environmental degrees of freedom in Eq. (1.19), and thereby obtain a master equation for the motion of the original system density matrix

$$\rho = \mathrm{Tr}_{env}(\rho_{tot}). \tag{1.21}$$

The most general trace-preserving and completely positive form of this evolution is the *Lindblad master equation* [21] for the reduced density matrix ρ

$$\frac{\partial \rho}{\partial t} = -\frac{i}{\hbar}[\hat{H}(t), \rho(t)] + \sum_n \frac{1}{2}\left[2\hat{C}_n \rho(t) \hat{C}_n^\dagger - \rho(t)\hat{C}_n^\dagger \hat{C}_n - \hat{C}_n^\dagger \hat{C}_n \rho(t)\right], \tag{1.22}$$

where the $\hat{C}_n = \sqrt{\gamma_n}\hat{A}_n$ are *collapse operators*, or Lindblad operators, and the operators $\hat{A}_n$ are derived from the interaction Hamiltonian $\hat{H}_{int}$, and γ_n are the corresponding rates. The Lindblad equation is derived assuming that: correlations of the system with the environment develop slowly, excitations of the environment caused by system decay quickly and terms that are fast-oscillating when compared to the system timescale of interest can be neglected. These three approximations are called *Born*, *Markov*, and *rotating wave*, respectively [22]. Since they do not hold for every system, e.g. a small environment that can be perturbed by the system, the Lindblad equation can be a wrong approximation and more advanced approaches should be used [23].

1.5 Compare noisy and ideal quantum processes

Since many real-world imperfections arise when a quantum process is performed, it is important to quantitatively measure these imperfections in order to characterize the quality of the quantum operation. In this section, we first introduce the description of quantum operations in the so-called operator-sum representation. Then, we briefly describe the procedure of quantum tomography used to determine the operators which characterize the quantum process. Once these operators have been determined, the quality of the quantum operation can be estimated. Different measures, which compare experiments with the theoretical ideal task, exist such as the average gate fidelity and the diamond error rate.

1.5.1 Operator-sum representation

The most general physical processes that may occur in a quantum system, including unitary evolution, measurement, noise, and decoherence, can be described by a *quantum operation* ε [24]. In this formalism, input ρ_{in} and output ρ_{out} states are related by

$$\rho_{\text{out}} = \varepsilon(\rho_{\text{in}}) = \sum_j \hat{E}_j \rho_{\text{in}} \hat{E}_j^\dagger, \tag{1.23}$$

where the operators $\hat{E}_j$ are known as *operation elements*, or Kraus operators [8], and obey the condition that $\sum_j \hat{E}_j^\dagger \hat{E}_j \leq 1$. As mentioned, the operation elements completely describe the effect of the process including any possible unitary operation (quantum logic gate), projection (generalized measurement), or environmental effect (decoherence).

1.5.2 Quantum process tomography

In an experiment, the quantum operation ε can be determined by using *quantum process tomography* [25]. The goal is to describe the state change process by determining the operators E_i which describe ε. To relate the E_i to measurable parameters, it is convenient to rewrite them in an orthogonal basis $\{\widetilde{E}_i\}$ for ρ

$$\hat{E}_i = \sum_m e_{im} \widetilde{E}_i, \tag{1.24}$$

where e_{im} can be complex. The Eq. (1.23) may thus be rewritten as

$$\varepsilon(\rho) = \sum_{m,n} \widetilde{E}_m \rho \widetilde{E}_n^\dagger \chi_{mn}, \tag{1.25}$$

where $\chi_{mn} = \sum_i e_{im} e_{in}^*$ is a positive Hermitian operator, also called *error correlation matrix*, and fully describes the action of the quantum process [26]. The big advantage of this representation is that once the basis $\{\widetilde{E}_i\}$ is chosen, the error correlation matrix can be shown to be unique to the process [24], namely it depends only on ε and not on the particular choice of operation element basis $\{\widetilde{E}_i\}$.

To determine χ from a set of measurement, a set of basis states $\{\rho_j\}$ is chosen, such that for each input state ρ_j, *quantum state tomography* returns an output

$$\varepsilon(\rho_j) = \sum_k c_{jk} \rho_k. \tag{1.26}$$

By defining $\widetilde{E}_m \rho_j \widetilde{E}_n^\dagger = \sum_k \beta_{jk}^{mn} \rho_k$ (where β_{jk}^{mn} is a complex matrix completely determined by the choice of the input basis states $\{\rho_j\}$, output basis states $\{\rho_k\}$ and the basis for the operators $\{\widetilde{E}_i\}$), one can note that $\sum_k \sum_{m,n} \chi_{mn} \beta_{jk}^{mn} \rho_k = \sum_k c_{jk} \rho_k$ and since β is invertible:

$$\chi_{mn} = \sum_{jk} (\beta^{-1})_{jk}^{mn} c_{jk}. \tag{1.27}$$

1.5.3 Average gate fidelity

The *average gate fidelity* F_{ave} compares how well an operation ε approximates an ideal gate $\hat{U}$ [27]. It is defined as

$$F_{\text{ave}}(\varepsilon, \hat{U}) = \int \mathrm{d}\psi \, \langle\psi| \hat{U}^\dagger \varepsilon(|\psi\rangle\langle\psi|) \hat{U} |\psi\rangle \, . \tag{1.28}$$

Note that $F_{\text{ave}} = 1$ if and only if ε implements $\hat{U}$ perfectly, while lower values indicate that ε is a noisy implementation of $\hat{U}$. Suppose we introduce an orthogonal basis of unitary operators $\{\hat{U}_j\}$ for the system, the average gate fidelity can be rewritten explicitly as

$$F_{\text{ave}}(\varepsilon, \hat{U}) = \frac{\sum_j \mathrm{Tr}\left(\hat{U}\hat{U}_j^\dagger \hat{U}^\dagger \varepsilon(\hat{U}_j)\right) + d^2}{d^2(d+1)} \tag{1.29}$$

where d is the system's dimension. In order to determine experimentally F_{ave}, the quantum process ε is determined through quantum process tomography and then it is substituted into Eq. (1.29).

1.5.4 Diamond distance

Let us consider two quantum operations ε_1 and ε_2 in the Hilbert space $\mathcal{H}$, the *diamond distance* [24] measures the distance between them, namely it measures how well we can distinguish between the two channels by applying them to input states of arbitrarily large dimensions [28]. By introducing an ancillary Hilbert space $\mathcal{K}$ and defining the input density matrix ρ in $\mathcal{K} \otimes \mathcal{H}$, the output states to discriminate are $(\mathbb{1} \otimes \varepsilon_1)(\rho)$ and $(\mathbb{1} \otimes \varepsilon_2)(\rho)$. The *diamond norm* is then defined as

$$\|\varepsilon_1 - \varepsilon_2\|_\diamond = \max_\rho \left(\|(\mathbb{1} \otimes \varepsilon_1)(\rho) - (\mathbb{1} \otimes \varepsilon_2)(\rho)\|_1 \right), \tag{1.30}$$

where $\|\cdot\|_1$ denote the trace norm. The *minimal error probability* reads

$$p_E = \frac{1}{2} - \frac{\|\varepsilon_1 - \varepsilon_2\|_\diamond}{4}. \tag{1.31}$$

The two quantum channels ε_1 and ε_2 become perfectly distinguishable ($p_E = 0$) when their diamond distance $\|\varepsilon_1 - \varepsilon_2\|_\diamond = 2$.

1.6 Quantum states at finite temperature

The thermal expectation value of an observable $\hat{A}$ in the canonical ensemble at temperature T is defined as

$$\langle \hat{A} \rangle_T = \mathrm{Tr}\left(\rho \hat{A}\right), \tag{1.32}$$

where ρ is the thermal density matrix at temperature T. In the canonical ensemble,

$$\rho = \frac{1}{Z} e^{-\beta \hat{\mathrm{H}}} \tag{1.33}$$

where $\beta = 1/k_B T$ with k_B the Boltzmann's constant and Z is the partition function.

By fixing an orthonormal basis $|i\rangle$, the expectation value of $\hat{A}$ can be rearranged in the following way [29]:

$$\begin{aligned} \langle \hat{A} \rangle_T &= \frac{1}{Z} \sum_i \langle i | \, e^{-\beta \hat{\mathrm{H}}/2} \hat{A} e^{-\beta \hat{\mathrm{H}}/2} \, | i \rangle \\ &= \frac{1}{Z} \sum_i P(i) \, \langle \phi(i) | \, \hat{A} \, | \phi(i) \rangle \, , \end{aligned} \tag{1.34}$$

where the set of normalized states $|\phi(i)\rangle$ is defined as

$$|\phi(i)\rangle = P(i)^{-1/2} e^{-\beta \hat{\mathrm{H}}/2} \, |i\rangle \tag{1.35}$$

together with the (unnormalized) probability distribution

$$P(i) = \langle i | \, e^{-\beta \hat{\mathrm{H}}} \, | i \rangle \, . \tag{1.36}$$

Let us fix as orthonormal basis state $|i\rangle$ the set of *classical product states* (*CPS*), with zero entanglement entropy, given by

$$|i\rangle = |i_1\rangle \, |i_2\rangle \, \ldots \, |i_N\rangle \, , \tag{1.37}$$

where the i_j label states in a local basis that may be chosen arbitrarily for each site j. At non zero β, we expect the resulting $|\phi(i)\rangle$ to have minimal entropy within this general class of states, and so we call them *minimally entangled typical thermal states* (*METTS*) [30].

1.6.1 Producing METTS with the pure-state method

The *pure-state method* is an approach for calculating METTS distributed with probability $P(i)/Z$ [29]. The steps of the algorithm are

1. Choose a CPS $|i\rangle$.
2. Compute the METTS by using Eq. (1.35).
3. Collapse a new CPS $|i'\rangle$ from $|\phi(i)\rangle$ with probability $p(i \to i') = |\, \langle i' | \phi(i) \rangle \,|^2$ and return to step 2.

Note that such a procedure could be carried out using any orthonormal basis of states $|i\rangle$, however not every choice would lead to an efficient algorithm.

Once the states $|\phi(i)\rangle$ are sampled, one may estimate the average value of the observable $\hat{A}$ at a finite temperature, $\langle \hat{A} \rangle_T$, by using Eq. (1.34). In the simulation described in detail in Chapter 4, METTS are sampled to simulate a finite trapping temperature of the atoms in optical tweezers.

Chapter 2

Quantum Computing with neutral atoms

"The best that most of us can hope to achieve in physics is simply to misunderstand at a deeper level."

— Wolfgang Pauli

Arrays of identical neutral atoms trapped in optical tweezers can be used to perform quantum computing. Neutral atoms boast several attractive features: they can readily be prepared by optical pumping in well-defined initial states, their qubit states can be accurately controlled with electromagnetic fields and precisely measured by using fluorescence. Moreover, in some cases they present long decoherence times since they can be well isolated from the environment [31]. Many atoms can be packed close together in a quantum computer since neutral atoms separated by more than a few angstroms interact very weakly. As already stated in Chapter 1, together with arbitrary single-qubit gates, the entangling operation forms a universal quantum computing gate set. However, to implement entangling gates strong interactions among qubits are required. Given the weak interaction between neutral atoms, a solution is to temporarily excite atoms to Rydberg states, i.e., a highly energetic state with exaggerated properties. In this way, the Rydberg blockade mechanism, which prevents more than one atom in a small volume from being simultaneously excited to a Rydberg state, can be used to entangle two qubits.

In Sec. 2.1, we describe the main properties of individuals Rydberg atoms making them very good tools for quantum computation. They benefit from their strong mutual interaction (given by huge dipole matrix elements) as well as their long lifetimes. Not less important, thanks to their simple internal structure they can be easily manipulated by means of currently available microwave technology. The scaling laws of the main properties with the principal quantum number are also

provided. Then, in Sec. 2.2 we describe the dipole-dipole interaction between two Rydberg atoms and we focus our attention on the Rydberg blockade mechanism. Finally, in Sec. 2.3 we explain how to write the system Hamiltonian of a neutral atom trapped in an optical tweezer and we describe the mechanism of atom-light interaction.

2.1 General properties of Rydberg atoms

Rydberg atoms are atoms with one or more electrons in a highly excited state with a principal quantum number $n^* \geq 10$. In such a state, the atom diameter is approximately a factor of 10^4 larger than that of a neutral atom in the ground state. However, the atom is not ionized, as its outer electrons are not free, but still bound, even if very weakly. This results in exaggerated properties of Rydberg atoms as their very high sensitivity to external electromagnetic influences and the strong interaction between them [32]. In the following, we will consider only atoms with a single valence electron.

2.1.1 Hydrogen atom approximation

In many scenarios, since the outer electron stays far away from the atomic core, it is sufficient to treat the Rydberg atom as hydrogenic [33]. This approach is the simplest model one can think of where the outer electron held by the Coulomb force orbits around an elementary charge. If we suppose the core as infinitely massive the Hamiltonian reads

$$\hat{\mathrm{H}}_0 = -\frac{\hbar}{2m_e}\boldsymbol{\nabla}^2 - \frac{q^2}{4\pi\varepsilon_0}\frac{1}{r}, \tag{2.1}$$

where m_e is the electron mass, q is the elementary charge and r is the core-electron distance. Its eigenfunctions are written as a product of radial and angular wavefunctions

$$\psi(r,\theta,\Phi) = R_{nl}(r)Y_l^{m_l}(\theta,\Phi). \tag{2.2}$$

The *radial* part can be expressed in terms of generalized Laguerre polynomials as

$$R_{nl}(r) = \sqrt{\left(\frac{2}{na_0}\right)^3 \frac{(n-l-1)!}{2n[(n+l)!]}}\, e^{-r/na_0}\left(\frac{2r}{na_0}\right)^l L_{n-l-1}^{2l+1}\left(\frac{2r}{na_0}\right), \tag{2.3}$$

where $a_0 \sim 0.529$Å is the Bohr's radius, while the *angular* wavefunction is a spherical harmonic function proportional to an associated Legendre polynomial and reads as

$$Y_l^{m_l}(\theta, \Phi) = N e^{i m_l \Phi} P_l^{m_l}(\cos\theta). \tag{2.4}$$

Each set of $\{n, l, m_l\}$ (respectively the *principal*, *orbital* and *magnetic* quantum numbers) describes a different wavefunction $|nlm_l\rangle$ and satisfies

$$n = 1, 2, 3, \ldots \tag{2.5a}$$
$$l = 0, 1, 2, \ldots, n-1 \tag{2.5b}$$
$$m_l = -l, -l+1, \ldots, 0, \ldots, l-1, l. \tag{2.5c}$$

In addition, the *spin* quantum number s represents the state of the electron and takes the value $s = \pm 1/2$, spin up and down respectively. The binding energy of the electron is given by the Rydberg formula

$$E_n^{(0)} = -\frac{R_\infty}{n^2}, \tag{2.6}$$

where $R_\infty = m_e q^4/(8\varepsilon_0^2 h^2) = 13.6$ eV is the Rydberg constant. To take into account the finite mass M of the atomic core, one has to replace R_∞ by $R_M = R_\infty/(1 + \frac{m_e}{M})$.

Fine structure correction

The next level of description includes the interaction between the electron spin and its motion; it is taken into account by using perturbation theory. The interaction hamiltonian is

$$\hat{\mathrm{H}}_{FS} = A\vec{\mathbf{L}} \cdot \vec{\mathbf{S}} \tag{2.7}$$

where $\vec{\mathbf{L}}$ and $\vec{\mathbf{S}}$ are the total orbital momentum and the total spin operators and the constant A represents the strength of the interaction. The total angular momentum operator is defined as

$$\vec{\mathbf{J}} = \vec{\mathbf{L}} + \vec{\mathbf{S}}. \tag{2.8}$$

Since the operators H, $\vec{\mathbf{L}}^2$, $\vec{\mathbf{S}}^2$, $\vec{\mathbf{J}}^2$ and J_Z all commute with each other, the set of eigenvalues $\{n, l, s, j, m_j\}$ completely specifies a unique eigenstate of the Hydrogenic atom $\left|nlsjm_j\right\rangle$. The possible values of j and m_j are

$$j = l \pm \frac{1}{2} \tag{2.9a}$$
$$m_j = -j, -j+1, \ldots, 0, \ldots, j-1, j. \tag{2.9b}$$

In addition to the spin-orbit coupling, the fine structure correction takes into account also relativistic corrections. In conclusion, the corrected binding energy within the fine structure picture is

$$E_{nlj} = E_n^{(0)}\left[1 + \frac{\alpha_F^2}{n}\left(\frac{1}{j+\frac{1}{2}} - \frac{3}{4n}\right)\right] \tag{2.10}$$

where $\alpha_F \sim 1/137$ is the fine structure constant and $E_n^{(0)}$ is given by Eq. (2.6).

Quantum defect theory

The assumption of the atomic core as a single point charge used previously holds as long as the outer electron is far away from the nucleus. For large n^*, this is valid for large l, but as soon as lower l are considered, as one can see in Fig. 2.1, there is a penetration of the outer electron into the electronic cloud of the core that has to be taken into account. Indeed, the presence of the outer electron close to the core leads to a deformation of the inner electronic cloud and the electron feels a deeper Coulomb potential due to a smaller screening of the nucleus charge. These effects lead to a reduction of the energy of the Rydberg state.

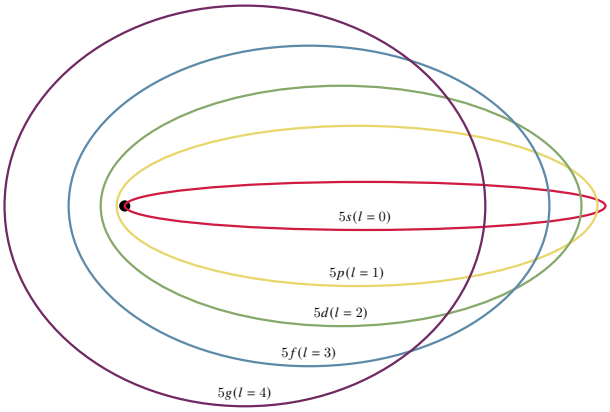

Figure 2.1 • Semiclassical orbits of the valence electron for an atom with $n = 5$ with all allowed values of orbital angular momentum. The black dot denotes the position of the atomic core.

A phenomenological approach to include this deviation is quantum defect theory which replaces the principal quantum number n by a non-integer effective quantum number $n^* = n - \delta_{l,j}$ where $\delta_{l,j}$ is the *quantum defect* which depends on the atomic species considered and on the angular momentum quantum numbers. Experimentally, the quantum defect can be obtained by measuring the binding energy of the electron according to

$$E_{nl} = -\frac{R_\infty}{1+\frac{m_e}{M}}\frac{1}{(n-\delta_{l,j})^2}. \tag{2.11}$$

2.1.2 Dipole matrix elements

The extreme sensitivity of Rydberg atoms to electric field derives from the huge matrix elements of the dipole operator. Given the dipole operator $\vec{\mathbf{d}} = -q\vec{\mathbf{r}}$, the dipole matrix elements between two levels $|nlm_l\rangle$ and $\left|n'l'm'_l\right\rangle$ is

$$\left\langle n'l'm'_l\right| \vec{\mathbf{d}} \left|nlm_l\right\rangle = -q \left\langle n'l'm'_l\right| \vec{\mathbf{r}} \left|nlm_l\right\rangle . \tag{2.12}$$

This dipole transition matrix is not zero only if the quantum numbers satisfy the *selection rules* given by

$$\Delta l = l - l' = \pm 1, \qquad \Delta m_l = m_l - m'_l = 0, \pm 1. \tag{2.13}$$

These transitions correspond to the emission or absorption of π polarized (Δm_l=0) photon or of a $\sigma^{\pm}$ polarized ($\Delta m_l = \pm 1$) photon. For low l Rydberg states, the dipole matrix element scales as $\sim n^2$ [32]. Thus, since Rydberg atoms have a high principal quantum number n, one can easily deduce that their dipole matrix elements are huge numbers. As a direct consequence, Rydberg atoms strongly couple to microwave radiation which can be used to manipulate transitions between Rydberg levels in real experiments. The scaling is different going towards $l \approx n$ where the dependency on the angular part has to be taken into account.

2.1.3 Radiative lifetime

The radiative decay from a state i to a state f of a Rydberg atom can be described by the Einstein coefficient A_{if} for spontaneous emission

$$A_{if} = \frac{\omega_{if}^3}{3\pi\varepsilon_0\hbar c^3} |\left\langle f\right| \vec{\mathbf{d}} \left|i\right\rangle|^2 \tag{2.14}$$

where ω_{if} is the transition frequency. The spontaneous decay rate γ_i of the level i is calculated by summing over all possible decay channels A_{if}, while the life-time is $t_i = 1/\gamma_i$. In general, the life-time scales as $\sim n^3$. This is not valid for $l \approx n$, where instead the scaling is as $\sim n^5$ [32].

At finite temperature, there is also a decay mechanism via the absorption and emission of blackbody radiation photons due to stimulation. The enhanced Einstein's coefficient is

$$B_{if} = \bar{n}(\omega) A_{if} \tag{2.15}$$

where $\bar{n}(\omega)$ is the mean number of photon per mode in free space at thermodynamic equilibrium. At finite temperature T, it is given by

$$\bar{n}(\omega) = \frac{1}{e^{\hbar\omega/k_B T} - 1}. \tag{2.16}$$

To give some numbers, the contribution from the stimulated transitions slightly reduces the lifetime of the rubidium atom in the 60s state from $244\,\mu$s at $0\,$K to $99\,\mu$s at room temperature [33].

2.1.4 Summary

As we have seen, Rydberg atoms possess exaggerated properties which scale rapidly with the principal quantum number n. Their size and dipole moment scale as n^2, while their radiative lifetime scale as n^3 and the binding energy as n^{-2}. These scaling laws are summarized in Tab. 2.1. As an example, the typical numbers for the rubidium atom in the 50p state are reported [34].

Property	Scaling	Rb(50p)
Binding energy E_n	n^{-2}	6.2 meV
Orbital radius r	n^2	$0.17\,\mu$m
Dipole moment	n^2	$3200\,ea_0$
Radiative lifetime t_a of $\|a\rangle$	n^3	$106\,\mu$s

TABLE 2.1 • Scaling behavior of some properties of Rydberg atoms with the principal quantum number n. These scaling laws refer to low l Rydberg states. The typical numbers for the rubidium atom in the 50p state are given [34].

2.2 Interacting Rydberg atoms

Let us consider two neutral atoms each having one electron excited into a Rydberg state and separated by a distance R. As long as R is much larger than the size of the electronic wavefunction, one needs to consider only the electrostatic interaction between two localized charge distributions utilizing the well-known electric multipole expansion in spherical coordinates [35]. It turns out that their interaction is mainly via the electric dipole-dipole operator

$$\hat{V}_{dd} \sim \frac{1}{4\pi\varepsilon_0|\vec{\mathbf{R}}|^3}\left(\vec{\mathbf{d}}_1\cdot\vec{\mathbf{d}}_2 - \frac{3(\vec{\mathbf{R}}\cdot\vec{\mathbf{d}}_1)(\vec{\mathbf{R}}\cdot\vec{\mathbf{d}}_2)}{|\vec{\mathbf{R}}|^2}\right) \tag{2.17}$$

where $\vec{\mathbf{d}}_i$ is the electric dipole moment of atom i. This approximation is valid in the near field of the oscillating dipole where the internuclear distance is considerably smaller than the wavelength of the transition.

The effect of this operator on a pair of Rydberg atoms depends on how the pair is prepared [33]. If the two atoms are excited in the same Rydberg level $|a\rangle$, $\hat{V}_{dd}$ has no effect at first order in perturbation theory as an atomic state has a vanishing

average electric dipole moment [16]. In this case, the dipole interaction operator acts as a second-order perturbation coupling to intermediate pair states $|cd\rangle$. If the dipole-dipole coupled states $|cd\rangle$ are not degenerate [36], the resulting interaction energy, and thus the shift of the considered pair state, has the form:

$$C_{aa} = \sum_{|cd\rangle} \frac{|\langle cd|\hat{V}_{dd}|aa\rangle|^2}{2E_a - E_c - E_d} = \frac{C_{6,aa}}{|\vec{\mathbf{R}}|^6} \tag{2.18}$$

corresponding to the Van der Waals interaction with $C_{6,aa}$ the *Van der Waals coefficient*. The latter scales dramatically with the principal quantum number as n^{11}. The Van der Waals interaction between two Rydberg atoms is huge: it can reach tens of megahertz for atomic separations of several micrometers.

2.2.1 The Rydberg blockade mechanism

The strong interaction between atoms excited to Rydberg states modifies the excitation dynamics. It can be exploited to suppress the simultaneous excitation of two atoms and to generate entangled states. This is obtained by driving atoms in a regime called *Rydberg blockade* [16].

Let us consider a resonant laser field that couples the ground state $|g\rangle$ and a given Rydberg state $|r\rangle$ with Rabi frequency Ω. In the case of two atoms separated by a distance $\vec{\mathbf{R}}$, the system is fully described by the states $|gg\rangle$, $|gr\rangle$, $|rg\rangle$, and $|rr\rangle$. The doubly excited state $|rr\rangle$ is shifted in energy by the quantity $C_6/|\vec{\mathbf{R}}|^6$ due to the van der Waals interaction. The Hamiltonian is of the form

$$\hat{\mathrm{H}} = \frac{\Omega}{2}(|g\rangle\langle r| \otimes \mathbb{1} + \mathbb{1} \otimes |g\rangle\langle r| + \mathrm{H.c.}) - \frac{C_6}{|\vec{\mathbf{R}}|^6}|rr\rangle\langle rr|\,. \tag{2.19}$$

Since the state $|-\rangle = (|gr\rangle - |rg\rangle)/\sqrt{2}$ does not take part in the dynamic, i.e. it is an eigenstate of the Hamiltonian with an eigenvalue of zero, the dynamics result as the one of a three-level system of states $|gg\rangle$, $|+\rangle = (|gr\rangle + |rg\rangle)/\sqrt{2}$ and $|rr\rangle$. In this new basis, the Hamiltonian becomes

$$\hat{\mathrm{H}} = \frac{\sqrt{2}\Omega}{2}(|gg\rangle\langle +| + |+\rangle\langle rr| + \mathrm{H.c.}) - \frac{C_6}{|\vec{\mathbf{R}}|^6}|rr\rangle\langle rr|\,. \tag{2.20}$$

Note the enhancement of the Rabi frequency by a factor of $\sqrt{2}$ in this basis. The resulting dynamics depend on the strength of the interaction compared to the Rabi frequency. In the regime of strong interactions denoted by $C_6/|\vec{\mathbf{R}}|^6 \gg \hbar\Omega$, that is $R_b \gg |\vec{\mathbf{R}}|$ where $R_b = (C_6/\hbar\Omega)^{1/6}$ is the blockade radius, the system behaves in the following way: the excitation from $|gg\rangle$ to the entangled state $|+\rangle$ is unaffected by the interaction. The excitation from $|+\rangle$ to $|rr\rangle$ is off-resonant because of the strong interaction. Effectively, the $|rr\rangle$ state is decoupled from the dynamics, as it can

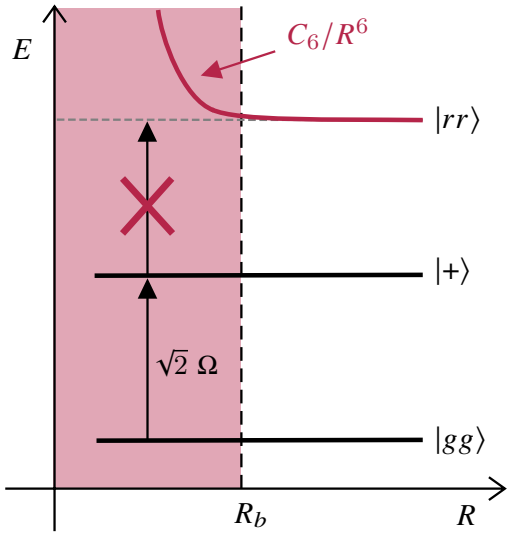

FIGURE 2.2 • For two-atoms separated by a distance $R < R_b$, the collective ground state $|gg\rangle$ is coupled only to $|+\rangle = (|gr\rangle + |rg\rangle)/\sqrt{2}$ with an enhanced Rabi frequency $\sqrt{2}\Omega$. The excitation from $|+\rangle$ to $|rr\rangle$ is shifted out of resonance by the Van der Waals interaction C_6/R^6.

never be reached. This decoupling of the doubly excited state is called the *Rydberg blockade*. Thus, in this case, the description can be reduced to the one of a two-level system consisting only of $|gg\rangle$ and $|+\rangle$, governed by the Hamiltonian

$$\hat{\mathrm{H}} = \frac{\sqrt{2}\Omega}{2}(|gg\rangle\langle +| + \mathrm{H.c.}). \tag{2.21}$$

The dynamics of this Hamiltonian produces Rabi oscillations as the non-interacting case. However, in this case the probability to find an atom in the Rydberg state p_r is given by

$$p_r(t) = \frac{1}{2}\sin^2(\sqrt{2}\Omega t) \tag{2.22}$$

and thus the maximum is given by $p_r = 1/2$, as the $|+\rangle$ state has only one of the two atoms in the Rydberg state.

The above considerations can be extended to an ensemble of N atoms all included within a blockade volume. For N atoms that can be either in the $|g\rangle$ or in the $|r\rangle$ state, the Hamiltonian can be written as

$$\hat{\mathrm{H}} = \frac{\Omega}{2}\sum_i \left(|g\rangle_i \langle r|_i + \mathrm{H.c.}\right) + \sum_{i<j} V_{ij}\,|r\rangle_i\,|r\rangle_j\,\langle r|_i\,\langle r|_j\,, \tag{2.23}$$

where V_{ij} is the strength of the van der Waals interaction between atoms i and j. In the blockaded regime, where all the interaction strengths are much larger than the Rabi frequency, i.e. $V_{ij} \gg \Omega$, at most one Rydberg excitation is possible. This leads to collective Rabi oscillations with an enhanced frequency $\sqrt{N}\Omega$

between the collective ground state $|G\rangle = |g_1 g_2 \dots g_N\rangle$ and the entangled state $|R\rangle = \frac{1}{\sqrt{N}} \sum_i |g_1 \dots r_i \dots g_N\rangle$ where the Rydberg excitation is shared among all the atoms. Indeed, in the collective basis, the Hamiltonian is given by

$$\hat{\mathrm{H}} = \frac{\sqrt{N}\Omega}{2}(|G\rangle\langle R| + \mathrm{H.c.}). \tag{2.24}$$

The probability to find an atom in the Rydberg state is given by

$$p_r(t) = \frac{1}{N}\sin^2(\sqrt{N}\Omega t). \tag{2.25}$$

In the case of a system whose size is larger than the blockade radius, several Rydberg atoms can be excited. The many-body dynamics will be very complex since the atom positions will be strongly correlated due to the blockade constraint.

2.3 Create assembling of neutral atoms array

2.3.1 Trapping in optical tweezers

In neutral atoms devices, the atoms are trapped in arrays by using optical tweezers. Their working principle is the following: the oscillating electric field of a light beam induces an oscillating electric dipole moment in the atom. The associated energy shift is called the AC Stark shift. When the light frequency is detuned from atomic resonance, little spontaneous emission occurs and the light creates a conservative potential for the atoms. Atoms are attracted to light below the resonance frequency (red detuned) and repelled by light above it (blue detuned). The optical tweezer is a red detuned laser beam that holds atoms at its focus [31]. The shape of the atom trap is the shape of the intensity field since the AC Stark shift is proportional to the light's intensity. The optical tweezers are typically approximated as harmonic traps since the tightly focused gaussian trapping beams of light give rise to an approximately harmonic trapping potential at the focus [37]. Thus, in the following, we will consider the trapping potential to be harmonic and we will work in 1-dimension.

Let us consider a single particle which can be in the electronic ground state $|g\rangle$ or in the excited state $|e\rangle$; the trapping contribution to the Hamiltonian of the system is

$$\hat{\mathrm{H}}_{\mathrm{trap}} = \frac{\hat{p}^2}{2m} \otimes \mathbb{1} + \frac{1}{2}m\hat{x}^2\Big(\omega_g^2 |g\rangle\langle g| + \omega_e^2 |e\rangle\langle e|\Big). \tag{2.26}$$

We can define the relative polarizability of $|g\rangle$ and $|e\rangle$ in terms of a fictitious trapping frequency ω as $\alpha_g = \omega_g^2/\omega^2$ and $\alpha_e = \omega_e^2/\omega^2$, respectively. If we fine-tune the wavelength of the trapping light, we can ensure that the optical polarizability

of the two states are identical. This is known as a *magic trapping condition* [38]. However, in general the polarizabilities of the two states are unequal. For instance, the Rydberg state it is generically not even trapped by the optical tweezer. Using ω, the Hamiltonian can be rewritten as

$$\hat{\mathrm{H}}_{\mathrm{trap}} = \left(\frac{\hat{p}^2}{2m} + \frac{1}{2}m\omega^2\hat{x}^2\right)\otimes\mathbb{1} + \frac{1}{2}m\omega^2\hat{x}^2\left((\alpha_g - 1)\,|g\rangle\langle g| + (\alpha_e - 1)\,|e\rangle\langle e|\right). \quad 2.27$$

Now let us expand the continuous position operators $\hat{x}$ and $\hat{p}$ in terms of the ladder operators as:

$$\hat{x} = \sqrt{\frac{\hbar}{2m\omega}}\left(\hat{a} + \hat{a}^\dagger\right) \quad 2.28a$$

$$\hat{p} = \sqrt{\frac{\hbar m\omega}{2}}\left(i\hat{a}^\dagger - ia\right) \quad 2.28b$$

which satisfy the commutation relation $[\hat{a}, \hat{a}^\dagger] = 1$ and also $\hat{a}\,|n\rangle = \sqrt{n}\,|n-1\rangle$ and $\hat{a}^\dagger\,|n\rangle = \sqrt{n+1}\,|n+1\rangle$. In this basis the Hamiltonian is given by:

$$\hat{\mathrm{H}}_{\mathrm{trap}} = \hbar\omega\left(\hat{N} + \frac{1}{2}\right)\otimes\mathbb{1} + \frac{\hbar\omega}{4}\left((\alpha_g - 1)\,|g\rangle\langle g| + (\alpha_e - 1)\,|e\rangle\langle e|\right)\left(\hat{a} + \hat{a}^\dagger\right)^2 \quad 2.29$$

where $\hat{N} = \hat{a}^\dagger\hat{a}$ is the number operator.

2.3.2 Atom-light interaction

Let us consider a two-level atom with ground state $|g\rangle$ and excited state $|e\rangle$ interacting with laser light. The light can be described by an oscillating electric field, e.g. a plane wave propagating in space $\vec{\mathbf{E}} = \vec{\mathbf{E}}_0\cos(\omega t - kx + \phi)$, with angular frequency ω, wave number k and phase ϕ [39]. The interaction between the atom and the field perturbs the energy of the atomic levels by an amount $\hat{\mathrm{H}}_{\mathrm{int}} = -\vec{\mathbf{d}}\cdot\vec{\mathbf{E}}$ where $\vec{\mathbf{d}} = \langle r|\,q\vec{\mathbf{r}}\,|g\rangle$ is the associated electric dipole moment of the transition between the levels $|g\rangle$ and $|e\rangle$ with q the charge and $\vec{\mathbf{r}}$ the position of the electron. The Hamiltonian for the system reads

$$\hat{\mathrm{H}} = \hbar\omega_g\,|g\rangle\langle g| + \hbar\omega_e\,|e\rangle\langle e| + \hbar\Omega\cos(\omega t - kx + \phi)(|g\rangle\langle e| + |e\rangle\langle g|), \quad 2.30$$

where we have introduced the *Rabi frequency* $\Omega = \vec{\mathbf{d}}\cdot\vec{\mathbf{E}}_0/\hbar$. For later convenience, we transform the Hamiltonian by introducing the frequency difference $\omega_{\mathrm{d}} = \omega_e - \omega_g$ as

$$\hat{\mathrm{H}} = -\frac{\hbar\omega_{\mathrm{d}}}{2}\,|g\rangle\langle g| + \frac{\hbar\omega_{\mathrm{d}}}{2}\,|e\rangle\langle e| + \hbar\Omega\cos(\omega t - kx + \phi)(|g\rangle\langle e| + |e\rangle\langle g|) \quad 2.31$$

where we ignore also the energy shift $\frac{\hbar\omega_g+\hbar\omega_e}{2}\mathbb{1}_2$. Then, the Hamiltonian of the two levels atom can be transformed by using the Euler formula, approximating $\cos\theta$ as [40]

$$\cos\theta = \frac{e^{i\theta}+e^{-i\theta}}{2} = \frac{e^{i\theta}}{2}\left(1+e^{-2i\theta}\right) \approx \frac{e^{i\theta}}{2}, \tag{2.32}$$

where we neglect $e^{-2i\theta}$ because $e^{-i\theta}$ goes away from $e^{i\theta}$ by two times speed. In general, fast oscillating terms may be neglected because on average $\int e^{in\theta}\,\mathrm{d}\theta \approx 0$ for large n. This is called *rotating wave approximation*. By recalling that the Hamiltonian is hermitian, we can approximate

$$\widetilde{\mathrm{H}} = -\frac{\hbar\omega_\mathrm{d}}{2}|g\rangle\langle g| + \frac{\hbar\omega_\mathrm{d}}{2}|e\rangle\langle e| + \frac{\hbar\Omega}{2}\left(e^{i(\omega t-kx+\phi)}|g\rangle\langle e| + e^{-i(\omega t-kx+\phi)}|e\rangle\langle g|\right). \tag{2.33}$$

The Hamiltonian can be rewritten within the rotating frame of reference [41] defined by the unitary transformation

$$\hat{\mathrm{H}}_\mathrm{rwf} = \hat{U}\widetilde{\mathrm{H}}\hat{U}^\dagger + i\hbar\frac{\partial\hat{U}}{\partial t}\hat{U}^\dagger, \tag{2.34}$$

where the unitary operator $\hat{U}(t)$ is given by

$$\hat{U}(t) = \begin{pmatrix} e^{-\frac{i(\omega t+\phi)}{2}} & 0 \\ 0 & e^{\frac{i(\omega t+\phi)}{2}} \end{pmatrix}. \tag{2.35}$$

The final Hamiltonian reads

$$\hat{\mathrm{H}}_\mathrm{rwf} = -\frac{\hbar\Delta}{2}|g\rangle\langle g| + \frac{\hbar\Delta}{2}|e\rangle\langle e| + \frac{\hbar\Omega}{2}\left(e^{-ikx}|g\rangle\langle e| + e^{ikx}|e\rangle\langle g|\right), \tag{2.36}$$

where we have defined the *detuning* of the laser relative to the transition frequency as $\Delta \equiv \omega_\mathrm{d} - \omega = \omega_e - \omega_g - \omega$.

Now, let us expand the continuous position variable x using Eq. (2.28a) and let us introduce the Lamb-Dicke parameter:

$$\eta = k\sqrt{\frac{\hbar}{2m\omega}} = \frac{2\pi}{\lambda}\sqrt{\frac{\hbar}{2m\omega}} \tag{2.37}$$

where λ is the wavelength of the driving laser. The final Hamiltonian in Eq. (2.36) becomes

$$\hat{\mathrm{H}}_\mathrm{rwf} = -\frac{\hbar\Delta}{2}|g\rangle\langle g| + \frac{\hbar\Delta}{2}|e\rangle\langle e| + \frac{\hbar\Omega}{2}\left(e^{-i\eta(\hat{a}+\hat{a}^\dagger)}|g\rangle\langle e| + e^{i\eta(\hat{a}+\hat{a}^\dagger)}|e\rangle\langle g|\right). \tag{2.38}$$

Gaussian incident beam

Now, let us consider a more realistic system by supposing that the incident light is a Gaussian beam. We suppose that the light propagates in the x direction and the focused beam intensity varies in y and z. Then the electric field of the beam [42] can be analytically modeled in three dimensions using

$$\vec{\mathbf{E}}(x,y,z,t) = |\vec{\mathbf{E}}_0|\frac{w_0}{w(x)}\exp\left[-\frac{(y^2+z^2)}{w^2(x)}\right] \times \exp\left[ik\frac{(y^2+z^2)}{2R(x)} - i\Phi(x)\right]e^{i(kx-\omega t)}, \tag{2.39}$$

where $|\vec{\mathbf{E}}_0|$ is the amplitude of the electric field at the center of the focal plan, w_0 is the *beam waist* and $w(x)$ is a function of axial distance from the plane of the beam waist

$$w(x) = w_0\sqrt{\left(1+\frac{x^2}{x_R^2}\right)}, \tag{2.40}$$

where we have defined *Rayleigh range* as $x_R = \pi w_0^2/\lambda$. The term $R(x)$ is the *wave-front curvature radius* and has the form

$$R(x) = x\left[1+\frac{x_R^2}{x^2}\right] \tag{2.41}$$

while $\Phi(x)$ is the *Gouy phase* given by

$$\Phi(x) = \tan^{-1}\left(\frac{x}{x_R}\right). \tag{2.42}$$

Given the electric field in Eq. (2.39), the system Hamiltonian illustrated in Eq. (2.36) can be modified in the following way [20]:

- → First of all, let us add the contribution given by the Guoy phase, so let us expand Eq. (2.42) in Taylor series as $\tan^{-1}(x/x_R) \approx x/x_R - x^3/3x_R^3$. The first linear term decreases the momentum kick along the beam axis $k \to k - 1/x_R$, but, typically, this relative change in the axial momentum can be ignored. Instead, the cubic term is taken into account with $\exp\left(-ix^3/3x_R^3\right)$.

- → Then, let us consider the contribution from the curvature of phase fronts. It is given by $\exp\left(\frac{-ix(y^2+z^2)}{x_R w_0^2}\right)$.

- → The focusing leads to a spatial dependence to the electric field strength. This is taken into account by adding the term $\exp\left(-\frac{x^2}{2x_R^2} - \frac{y^2+z^2}{w_0^2}\right)$.

In conclusion, the Hamiltonian of atom-light interaction with the light modeled as a Gaussian beam can be rewritten as

$$\hat{\mathrm{H}}_{\mathrm{rwf}} = -\frac{\hbar\Delta}{2}\left|g\right\rangle\!\left\langle g\right| + \frac{\hbar\Delta}{2}\left|e\right\rangle\!\left\langle e\right| + \frac{\hbar\Omega}{2}\left(e^{\mathrm{G}_g}\left|g\right\rangle\!\left\langle e\right| + e^{-\mathrm{G}_g}\left|e\right\rangle\!\left\langle g\right|\right) \tag{2.43}$$

where

$$\mathrm{G}_g = -ikx - \frac{ix^3}{3x_R^3} - \frac{ix(y^2+z^2)}{x_R w_0^2} - \frac{x^2}{2x_R^2} - \frac{y^2+z^2}{w_0^2}. \tag{2.44}$$

This equation is the reference point for Subsec. 4.2.2 to write the atom-light interaction part of the Hamiltonian of a system composed of two neutral atoms in the quantum register.

Chapter 3

An algorithm for Optimal Control: dCRAB

"Or does it mean, as it seems to me, that we must accept the idea that reality is only interaction?"

— Carlo Rovelli

In the last years, one of the most promising challenges in physics is the capability to control quantum systems. For this purpose, there is an increasing interest in quantum optimal control (OC) theory that studies the development of optimization techniques to improve the outcomes of quantum processes [18, 43]. An optimization method to compute the optimal driving fields, to let the system evolve from an initial to a target state, is the *dressed Chopped Random Basis* (dCRAB) technique. Its key feature is to expand the control function into a sum of truncated randomized basis and the problem is recast to a multi-variable function minimization that can be performed via direct-search methods. This algorithm can be used both in an open-loop and in a closed-loop optimization and it is capable to work under experimental constraints.

In Sec. 3.1, the key idea and structure of the dCRAB algorithm are discussed. Then, in Sec. 3.2, we briefly describe the quantum optimal control suite which incorporates the algorithm and is used for the gate optimization in Chapter 5.

3.1 Algorithm description

3.1.1 Control problem

In order to explain the working principles of the dCRAB algorithm [18], one has to define a *control problem*. The simplest problem one can think of is the *state-to-state transfer*. Let us consider an initial state $|\psi_0\rangle$ whose evolution is described by $|\psi(t)\rangle = U(t)\,|\psi_0\rangle$, where the unitary operator $U(t)$ is the solution of the Schrödinger equation with Hamiltonian:

$$\hat{\mathrm{H}}(t) = \hat{\mathrm{H}}_0 + f(t)\hat{\mathrm{H}}_1 \tag{3.1}$$

where $\hat{\mathrm{H}}_0$ is the *drift* Hamiltonian, while $\hat{\mathrm{H}}_1$ is the *control* Hamiltonian with $f(t)$ a time-dependent *control pulse*. Our aim is to transfer the state from the initial $|\psi_0\rangle$ to $|\Phi\rangle$ in a time T. Let us set the *control objective* $J(f)$ to be the overlap of the time evolved state and the target state, namely the fidelity of the state transfer:

$$J(f) = F(|\psi(T)\rangle) = |\langle\Phi|\psi(T)\rangle|^2 \tag{3.2}$$

The *control problem* is finding a control pulse $f(t)$ in order to maximize $J(f)$.

3.1.2 Key idea

The key idea of the dCRAB algorithm to tackle the control problem is an iterative procedure consisting of N_s *super-iterations*. For each super-iteration j, the control pulse $f^j(t)$ is expanded in a truncated randomized basis with N_c basis functions $f_i^j(t)$ and the coefficients c_i^j $(i = 0, \ldots, N_c)$ are optimized. Then, the optimal solution from the previous superiterations is used as a guess pulse for the next iteration. Thus, the control pulse in the j-th super-iteration can be written as:

$$f^j(t) = c_0^j f^{j-1}(t) + \sum_{i=1}^{N_c} c_i^j f_i^j(t) \tag{3.3}$$

where $f_i^j(t)$ are the new basis functions and f^{j-1} is the control pulse obtained from the $(j-1)$-th super-iteration. As one can note, the coefficient c_0^j allows the optimization to move along the direction of the old pulse, while the coefficients c_i^j allow it to move along the new search directions $f_i^j(t)$. This is a crucial step to escape from local false traps.

3.1.3 Constrained optimization

With the dCRAB algorithm one can also perform *constrained optimizations*. Bandwidth constraints are naturally introduced in the truncated randomized basis expansion choice, but also other types of constraints can be implemented:

→ a *hard wall* constraint can be imposed to limit the pulse height to a maximum value $f_{\max}$. The update formula becomes:

$$f^j(t) = \begin{cases} \tilde{f}^j(t) & \text{if } \left|\tilde{f}^j(t)\right| < f_{\max} \\ \text{sign}(f^j(t))\, f_{\max} & \text{otherwise} \end{cases} \tag{3.4}$$

where $\tilde{f}^j(t)$ is as in Eq. (3.3). This hard wall constraint can potentially increase the bandwidth of the control pulse.

→ alternatively, if one desires to maintain the bandwidth constraint while introducing an additional hard wall constraint, a *rescaling* of the control pulse at each iteration can be performed. In this way, the pulse maximum is limited to $f_{\max}$ but its shape is not affected. The update formula becomes:

$$f^j(t) = \begin{cases} \tilde{f}^j(t) & \text{if } \tilde{f}^j_{\max}(t) < f_{\max} \\ \frac{f_{\max}}{\tilde{f}^j_{\max}} \tilde{f}^j(t) & \text{otherwise} \end{cases} \tag{3.5}$$

where $\tilde{f}^j_{\max} = \max_t |\tilde{f}^j(t)|$ and $\tilde{f}^j(t)$ is as in Eq. (3.3).

Quantum Speed Limit

Whether or not a solution of the control problem can be found, depends on the available resources as the finite pulse operation time, the finite pulse power as well as the degrees of freedom of the control pulse,e.g., given by the bandwidth or parametrization of the control pulse. In particular, the minimum pulse time is limited by the pulse power by a condition commonly known as the *Quantum Speed Limit* (*QSL*) closely related to time-energy uncertainty relations.

As an example of QSL, for closed quantum systems with unitary time evolution, the minimum evolution time between two distinguishable states of a quantum system is limited by the Mandelstam–Tamm [44] bound

$$T_{\text{QSL}} \geq \frac{\pi\hbar}{2\Delta E} \tag{3.6}$$

where ΔE is the variance of energy of the initial state.

3.2 Quantum optimal control suite

The *quantum optimal control suite* (*QuOCS*) is an open source software for optimal control written in Python. It incorporates the algorithm dCRAB for performing both open- and closed-loop optimizations. In the following, we give a brief overview of the main optimization options that one can set. These options will be chosen carefully to perform the two-qubit CZ gate optimization in Chapter 5.

Main settings

The dCRAB algorithm can be selected and the minimization of the figure of merit can be performed through the Nelder-Mead method. It is a direct search method thus it does not require the computation of any gradient. The number of superiterations N_s and the number of iterations N, for each superiteration, should be fixed as well as the total duration of the pulses T.

Pulses

Multiple pulses may be defined and for each of them the truncated basis with N_c basis functions is selected. For instance, one can choose the Fourier basis given by

$$f(t) = \sum_{i=1}^{N_c} \left[A_i \sin\left(\frac{2\pi\omega_i t}{T}\right) + B_i \cos\left(\frac{2\pi\omega_i t}{T}\right) \right] \tag{3.7}$$

For each superiteration, the set of frequencies $\{\omega_i\}$ of dimension N_c are randomly sampled following a uniform distribution between the upper and lower limit, $\omega_{\max} = 2\pi n_{\max}/T$ and $\omega_{\min} = 2\pi n_{\min}/T$ respectively. For each iteration, the $2N_c$ parameters given by $\{A_i\}$ and $\{B_i\}$ are optimized. By imposing hard wall constraints, the pulse amplitudes can be limited to a maximum and minimum values, $f_{\max}$ and $f_{\min}$. An initial guess for the pulses can be given in input as well as a maximum amplitude variation for the first iteration.

Parameters

Multiple parameters may be also optimized and for each of them an initial guess should be given in input. The value of each parameter can be bounded between a lower and upper limit. Moreover, an initial amplitude variation can be provided.

Part II

Simulation and optimization of two-qubit CZ gate

Chapter 4

Setup and Methods

"Nature isn't classical, dammit, and if you want to make a simulation of Nature, you'd better make it quantum mechanical, and by golly it's a wonderful problem, because it doesn't look so easy."

— Richard Feynman

In this Chapter, a brief overview of the experimental apparatus at the basis of a neutral atom quantum processor is given in Sec. 4.1. By reference to a general processor, the main ideas of the QRydDemo apparatus are also presented. After that, in Sec. 4.2 the total Hamiltonian of two-atoms in the quantum register is shown and the different contributing terms are analyzed. Then, we describe a software which performs a simulation of this system in order to reproduce the behavior of a two-qubit CZ gate. This software has been developed by Sebastian Weber within the QRydDemo project.

4.1 Neutral atom quantum processor

The neutral atom quantum processor is based on configurable arrays of single neutral atoms. The array can be seen as a *register*, where each single atom plays the role of a qubit. Two electronic levels of the neutral atom are chosen to be the two-qubit states, which we refer to as $|0\rangle$ and $|1\rangle$. Since the register in an atomic quantum processing unit is not permanently built, a typical computation cycle consists of three phases: register preparation, quantum processing, and register readout [12]. In this section, after illustrating the atomic levels involved in the QRydDemo quantum processor, we will briefly review the building blocks of these three stages for this platform.

4.1.1 Atomic levels

The main idea of the QRydDemo project is to use a Strontium-88 platform but encode the qubit in a way that so far has not been demonstrated using this isotope. On the valence structure, the Strontium atom has two valence electrons [45]. As we can see in Fig. 4.1, there is a strong transition at 461 nm that can be used for cooling the atoms and for *fluorescence detection*. There is also a transition at 689 nm between the singlet and triplet sectors that can be used for sidebands cooling. The idea is to encode the *qubit* in this metastable triplets state, in particular in the two very long-lived ones $5s5p^3P_0$ for $|0\rangle$ and $5s5p^3P_2$ for $|1\rangle$. The two states can be connected using fast Raman transfer incorporating the intermediate state $5s6s^3S_1$. Diode lasers can be used to make fast Raman gates on 100 ns time scale. The Rydberg manifold can be reached by a single-photon transition using light at 323 nm. A single-photon transition allows one to get rid of spontaneous scattering on an intermediate state in comparison with two-photon excitation.

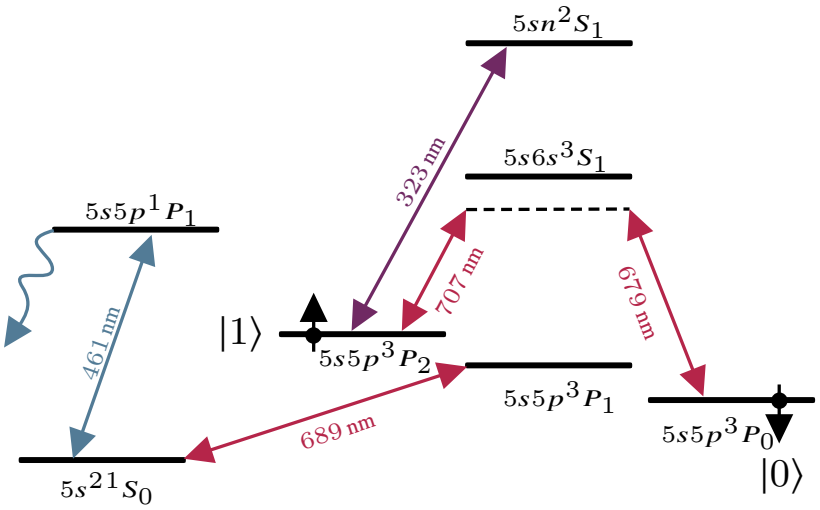

FIGURE 4.1 • Atomic levels of Strontium-88 involved in the encoding of the qubit and on the implementation of quantum gates. The transitions between the atomic levels with their relative wavelengths are represented with the colored arrows.

4.1.2 Register loading

As a starting point, a dilute atomic vapor is formed inside an ultra-high vacuum system operated at room temperature. Then, a cold ensemble of atoms is prepared inside a 3D magneto-optical trap. To prepare a register made of neutral atoms, a second trapping laser system isolates individual atoms within this ensemble: the Strontium-88 atoms are trapped in optical tweezers in $2D$ *arrays* with a typical

spacing of the order of $\sim 1\,\mu$m. Within a trapping volume of a few μm^3, each tweezer contains at most one single atom at a time. The size of the quantum register is only limited by the amount of trapping laser power and by the performance of the optical system generating the optical tweezers. In principle, this confers the property of *scalability* to neutral atom platforms.

The tweezer loading is a *stochastic process*, namely on average there is a 50% chance that after the loading of the magnetic optical trap a site is empty or filled by exactly one atom. To detect which of the tweezers are filled, the atoms are imaged by collecting their fluorescence onto a sensitive camera. After the occupied sites are specified, the atoms are shifted in order to generate the desired sub-registers. At the end of the shift operations, an assembled image is acquired to confirm the new positions of the atoms in the sub-register.

Optical tweezers implementation

The optical tweezers are technically realized using Acusto Optic Deflectors (AODs) which deflect an input beam into hundreds of beams. Indeed, in the operation of an AOD the power driving the acoustic transducer is kept on, at a constant level, while n different radio frequency (RF) tones $\{\omega_1, \ldots, \omega_n\}$ are applied in order to generate n beams with output angles $\{\theta_1, \ldots, \theta_n\}$, where $\theta_i = \theta(\omega_i)$. This step allows us to prepare one-dimensional arrays that can be shifted in 100 ns time scale by changing the frequencies that one fits onto the AODs. The plan is to use up to 20 AODs, stack them together and build a 2D array of individually controlled 1D lines each of them with about ~ 50 traps. The target is to reach on the order of 500 shiftable qubits allowing for fast and individually (decoupled) control over each atom in this 2D array.

The crucial idea at the basis of the QRydDemo device is using trapping at 592 nm for the tweezer arrays. This generates a *magic trapping condition* (see Sec. 2.3) for the qubit states, $|0\rangle$ and $|1\rangle$, and the Rydberg state $|r\rangle$. This aspect is really important working with neutral atoms since they typically present very strong dipole forces which generate dephasing of the qubit state while they are trapped in the arrays. So, one has to work on specific wavelengths where the traps look the same for all the involved states as the triple magic point. This in principle would allow for a target coherence time of the order of 10 ms and that would be a 10^3 improvement compared to what has been demonstrated so far [13]. Once these long coherence times are reached, one can think about doing more complex operations on these atoms arrays as manipulating the atom's position within the single-atom coherence time of the system. Up to now, the shuffling time using AOD systems typically takes on the order of $100\,\mu$s and thus there is a trade-off of how often an array can be reshuffled. With the target coherence time, more operations can be implemented and this offers the possibility to explore new types of algorithms.

Tweezers calibration

As already pointed out, a proper realization of the optical tweezers has a direct and crucial impact on the performance of the neutral atom processor. In this paragraph, we will analyze how to calibrate the tweezers in order to address the trap homogeneity.

The waveform that one initially sends into the AOD has the form:

$$\sum_{i=1}^{n} A_i e^{i\phi_i} e^{i\omega_i t} \tag{4.1}$$

with A_i and ϕ_i being the real amplitude and phase, respectively, of the radio frequency tone with frequency ω_i. The finite power bandwidth along with other imperfections of the system, given for instance by the RF amplifier and the AOD, generate a *non-linear response* to the input signal [46]. For instance, at the lowest order of non-linearity, new tones are generated as the difference and sum of the input frequencies. At the next order, these new tones are mixed with the original ones. Thus, these intermodulations can interfere destructively with the original tones if the set of phases $\{\phi_i\}$ are not carefully selected. To address this issue, the phases of the different RF tones are chosen to almost completely cancel out the non-linearities. By starting with n tones evenly spaced in frequency and with random phases and equal amplitudes, each phase in the set $\{\phi_i\}$ is optimized by minimizing the quantity

$$\sum_{\substack{i,j \\ i \neq j}} A_i e^{i(\phi_i - \phi_j)} e^{i(\omega_i - \omega j)t} \tag{4.2}$$

After the phases calibration, the amplitudes should be adjusted in order to realize homogeneous traps. Thus, the next step in the optimization consists of imaging the focused trap array on a camera and find the intensity peaks. The amplitudes are consequently modified in order to minimize the difference in intensity between all the peaks. For doing that an iterative procedure, consisting of taking an image and adjusting the amplitude, is exploited until all the intensity peaks are approximately uniform.

In Fig. 4.2 an image of a tweezer array with 100 traps, implemented for the QRydDemo experiment, is shown before and after we perform the calibration of the phases and amplitudes. One can see that before the adjustment the intermodulations strongly interfere with the intended frequency tones and significantly distort the trap amplitudes. Instead, by optimizing the phases $\{\phi_i\}$ and amplitudes $\{A_i\}$ of the RF tones one can reduce intermodulations and generate homogeneous traps.

FIGURE 4.2 • Tweezer array with 100 traps before (up) and after (down) we perform the calibration of the phases and the amplitudes.

4.1.3 Quantum processing

Once the register is fully assembled, quantum processing can start. In the processing stage a succession of gates, described by a quantum circuit, is applied to the qubits to implement a quantum algorithm. The quantum gates are realized by shining fine-tuned laser pulses onto a chosen subset of individual atoms in the register. Since the spacing between atoms in the register is of the order of $\sim$ μm, specific qubits can be addressed with high accuracy by strongly focusing the lasers. As already discussed in Sec. 1.2, one- and two-qubit gates are all that is needed to constitute a universal gate set.

In order to reach any point on the Bloch sphere and thus implementing any single-qubit gate, arbitrary rotation around the x- and z-axis should be performed. In the QRydDemo platform, rotation around the x-axis by an arbitrary angle will be performed by driving the qubit transition with a control field. The latter is an optical laser field coupling $|0\rangle$ $(5s5p^3P_0)$ and $|1\rangle$ $(5s5p^3P_2)$ via Raman transitions through the intermediate atomic state $5s6s^3S_1$ [47]. The atom-light interaction is characterized by the Rabi frequency Ω. The pulse duration defines the rotation angle, namely driving the control field for a duration τ induces a rotation around the x-axis with an angle $\Omega\tau$. Instead, rotation around the z-axis by an arbitrary angle will be performed via AC Stark shift.

To implement two-qubit gates strong interactions among qubits are required. Since neutral atoms separated by more than a few angstroms interact very weakly, a solution is to temporarily transfer atoms to Rydberg states, as already discussed in Chapter 2. In this way, the Rydberg blockade mechanism can be exploited to entangle two qubits. It is the basic mechanism to achieve a quantum logic: the excitation of a first atom to a Rydberg state conditions the excitation of a second one. Since there are never two simultaneous Rydberg excitations, the atoms are never subjected to significant forces on each other even as they become entangled. Moreover, since the Rydberg interaction is strong and long-range, it is possible to entangle not just neighboring atoms but also those separated by several lattice

sites. Furthermore, the distance between atoms in the optical tweezers is ideally suited to be combined with the interaction between Rydberg atoms since the typical interaction strength is of the order of MHz and allows one to drive gates on the order of $100\,\mathrm{ns}$ time-scale. Technically, the entangling gates are realized by driving the two targeted atoms with a control field generated by an arbitrary waveform generator which can produce pulses $\sim A(t)\sin(\omega_{\mathrm{RF}}(t)t + \phi(t))$. In practice, a radio frequency is added on top of the optical frequency and this allows one to tune the amplitude and the phase of the pulse. The laser-light interaction, in the rotating wave frame, is characterized by the Rabi frequency Ω, the detuning Δ and their relative phase ϕ. By tuning the pulses duration τ and these parameters, two-qubit gates can be realized.

4.1.4 Register readout

After the execution of quantum algorithms, the atomic register is read out by taking a final fluorescence image. The image is acquired with a sensitive camera and the acquisition is performed such that each atom in qubit state $|0\rangle$ will appear as bright, whereas atoms in qubit state $|1\rangle$ remain dark.

As imposed by quantum mechanics, the possible outcomes are probabilistic. Thus, the three computation cycles are repeated many times in order to reconstruct the relevant statistical properties of the final quantum state produced by the algorithm. The temporal sequence of one computation cycle is depicted in Fig. 4.3.

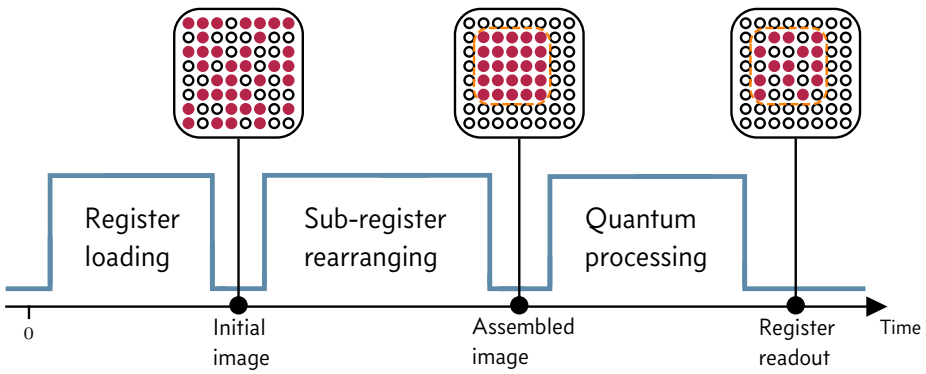

Figure 4.3 • Temporal sequence of one computation cycle for a neutral atom quantum processor. The loading of the register is a stochastic process, i.e. there is a 50% probability that after the loading a trap is empty or filled by one atom. The atoms are rearranged to realize the desired sub-registers, on which the quantum processing is performed.

4.2 Hamiltonian of two neutral atoms in the register

Let us consider a system composed of two neutral atoms of the quantum register discussed in Subsec. 4.1.2. The atoms are trapped in optical tweezers and each of them can be in the qubit states $|0\rangle$ and $|1\rangle$. In order to interact, the atoms can be excited to the Rydberg state $|r\rangle$. From now on, for simplicity, we will suppose $\hbar = 1$. The total Hamiltonian of the system can be written in a rotating-wave frame as

$$\begin{aligned}\hat{\mathrm{H}}_{\mathrm{tot}} = &\hat{\mathrm{H}}_{\mathrm{trap}} \otimes \mathbb{1} + \mathbb{1} \otimes \hat{\mathrm{H}}_{\mathrm{trap}} \\ &+ \Omega(\hat{\mathrm{H}}_{1r} \otimes \hat{\mathrm{R}}) + \Omega^*(\hat{\mathrm{H}}_{1r} \otimes \hat{\mathrm{R}})^\dagger + \Omega(\hat{\mathrm{R}} \otimes \hat{\mathrm{H}}_{1r}) + \Omega^*(\hat{\mathrm{R}} \otimes \hat{\mathrm{H}}_{1r})^\dagger \\ &+ \Delta(\hat{\mathrm{H}}_r \otimes \mathbb{1}) + \Delta(\mathbb{1} \otimes \hat{\mathrm{H}}_r) + \hat{\mathrm{H}}_{\mathrm{inter}}\end{aligned} \tag{4.3}$$

where $\hat{\mathrm{H}}_{\mathrm{trap}}$ describes the *optical traps* with the atoms polarization inside it. $\hat{\mathrm{H}}_{1r}$ define the *coupling* between the state $|1\rangle$ and $|r\rangle$ driven by the Rabi frequency Ω and $\hat{\mathrm{R}}$ is the restrictor operator which, as we will see, has a different form depending if a perfect or imperfect blockade regime is considered. Then, $\hat{\mathrm{H}}_r$ describes the *detuning* of the Rydberg state and $\hat{\mathrm{H}}_{\mathrm{inter}}$ identifies the *Rydberg atoms interaction*.

4.2.1 Trapping part

As shown in Subsec. 2.3.1, to reproduce the trapping by the optical tweezers the latter can be modeled as one-dimensional harmonic oscillators with trapping frequency ω

$$\frac{\hat{\mathrm{H}}_{\mathrm{trap}}}{2\pi} = \omega\left(\hat{N} + \frac{1}{2}\right) \otimes \mathbb{1} + \hat{\mathrm{H}}_{\mathrm{polar}} \tag{4.4}$$

where $\hat{N}$ is the number operator, whose dimension depends on the number of energy levels n taken into account, and $\hat{\mathrm{H}}_{\mathrm{polar}}$, which describes the relative polarizabilities of the electronic states of the atom inside the trap, is given by

$$\hat{\mathrm{H}}_{\mathrm{polar}} = \frac{\omega}{4}[(\alpha_0 - 1)\,|0\rangle\langle 0| + (\alpha_1 - 1)\,|1\rangle\langle 1| + (\alpha_r - 1)\,|r\rangle\langle r|] \otimes \left(a + a^\dagger\right)^2 \tag{4.5}$$

where α_0, α_1 and α_r are the relative polarizabilities of the states $|0\rangle$, $|1\rangle$ and $|r\rangle$ respectively. For satisfying the *magic trapping condition*, one should impose $\alpha_0 = \alpha_1 = \alpha_r$.

In order to reproduce the optical tweezer potential in 3D, one can consider an independent harmonic oscillator along the three axis x, y and z [37]. Thus, for each trap, one can suppose a harmonic oscillator in the axial direction with n_{ax} oscillator levels and trapping frequency ω_{ax}, one in the transverse direction (along

the interatomic axis) with n_{ta_1} and ω_{ta_1} and one in another transverse direction with n_{ta_2} and ω_{ta_2}. Consequently, the dimension of the Hilbert space of the system with two atoms is $(n_s n_{ax} n_{ta_1} n_{ta_2})^2$, where $n_s = 3$ is the number of electronic states of each atom.

4.2.2 Atom-light interaction part

Following the theoretical formulation of atom-light interaction developed in Subsec. 2.3.2, the Hamiltonian which describes the coupling of the single atom on the $|1\rangle \leftrightarrow |r\rangle$ transition is

$$\frac{\hat{\mathrm{H}}_{1r}}{2\pi} = \frac{1}{2}\,|r\rangle\langle 1| \otimes e^{\mathrm{G}} \tag{4.6}$$

where the exponential factor e^G depends on whether we suppose the incident light to be a plane wave or a Gaussian beam:

→ If the light is treated as a *plane-wave* and one supposes also to have a laser misalignment x_{ax} along the axial direction, the exponential factor is

$$\mathrm{G}_p = -i\eta_{1e_{ax}}\left(\hat{a}_{ax} + \hat{a}_{ax}^{\dagger} - x_{ax}\right)/x_{0_{ax}} \tag{4.7}$$

where $x_{0_{ax}} = \sqrt{\hbar/(4\pi m\omega_{ax})}$ and $\eta_{1e_{ax}} = 2\pi x_{0_{ax}}/\lambda_{1r}$ is the Lamb-Dicke parameter, with λ_{1r} the transition wavelength from $|1\rangle$ to $|r\rangle$ and m the atom mass.

→ If the light is treated as a *Gaussian-beam*, and one supposes a laser misalignment x_{ax} along the axial direction of beam propagation and x_{ta_1} and x_{ta_2} along the transverse ones (along with the focused beam varies in intensity), the exponential factor becomes

$$\begin{aligned}
\mathrm{G}_g = \mathrm{G}_p &- i\left(x_{0_{ax}}(\hat{a}_{ax} + \hat{a}_{ax}^{\dagger}) - x_{ax}\right)^3 \frac{1}{3z_{0_{1e}}^3} \\
&- i\left(x_{0_{ax}}(\hat{a}_{ax} + \hat{a}_{ax}^{\dagger}) - x_{ax}\right)\left(x_{0_{ta_1}}(\hat{a}_{ta_1} + \hat{a}_{ta_1}^{\dagger}) - x_{ta_1}\right)^2 \frac{1}{z_{0_{1e}} w_0^2} \\
&- i\left(x_{0_{ax}}(\hat{a}_{ax} + \hat{a}_{ax}^{\dagger}) - x_{ax}\right)\left(x_{0_{ta_2}}(\hat{a}_{ta_2} + \hat{a}_{ta_2}^{\dagger}) - x_{ta_2}\right)^2 \frac{1}{z_{0_{1e}} w_0^2} \\
&- \left(x_{0_{ax}}(\hat{a}_{ax} + \hat{a}_{ax}^{\dagger}) - x_{ax}\right)^2 \frac{1}{2z_{0_{1e}}^2} \\
&- \left(x_{0_{ta_1}}(\hat{a}_{ta_1} + \hat{a}_{ta_1}^{\dagger}) - x_{ta_1}\right)^2 \frac{1}{w_0^2} \\
&- \left(x_{0_{ta_2}}(\hat{a}_{ta_2} + \hat{a}_{ta_2}^{\dagger}) - x_{ta_2}\right)^2 \frac{1}{w_0^2}
\end{aligned} \tag{4.8}$$

where $z_{0_{1e}} = \pi w_0^2/\lambda_{1r}$ is the Rayleigh range and w_0 is the beam waist.

Now, let us analyze the restrictor operator $\hat{\mathrm{R}}$:

→ In the real world, the Rydberg blockade condition $C_6/R^6 \gg \hbar\Omega$ (see Subsec. 2.2.1) is only partially fullfilled and a regime of *imperfect Rydberg blockade* holds. To take into account finite blockade interactions, i.e. a dynamics toward the state $|rr\rangle$, the restrictor operator is just the identity.

→ If a *perfect Rydberg blockade* regime is assumed, the $|rr\rangle$ is decoupled from the dynamics. The operator is:

$$\hat{\mathrm{R}} = (|0\rangle\langle 0| + |1\rangle\langle 1| + |d\rangle\langle d|) \otimes \mathbb{1} \tag{4.9}$$

where, as we will see later, $|d\rangle$ is a generic state outside the computational basis which takes into account the *finite lifetime* of the Rydberg state.

Finally, the detuning Hamiltonian is simply given by:

$$\frac{\hat{\mathrm{H}}_r}{2\pi} = |r\rangle\langle r| \tag{4.10}$$

4.2.3 Rydberg atoms interaction part

Two neutral atoms excited to the Rydberg state $|r\rangle$ interact mainly via dipole-dipole interaction, as discussed in Sec. 2.2. If the two atoms are excited to the same Rydberg level, the resulting interaction energy has the form

$$\frac{\hat{\mathrm{H}}_{\mathrm{inter}}}{2\pi} = -\frac{C_6}{R^6}|rr\rangle\langle rr| \tag{4.11}$$

where C_6 is the Van der Waals coefficient and R is the distance between the two atoms.

4.3 Numerical simulation

The total Hamiltonian in Eq. (4.3) is numerically implemented in Python by Sebastian Weber within the QRydDemo project to reproduce the behavior of a two-qubit CZ gate (see Sec. 1.2) which exploits the Rydberg blockade effect. His program takes in input the time evolution array, the Rabi frequency array Ω, the detuning Δ and the rotation of the driving field ξ such that $\Omega \to e^{i\xi}\Omega$. Realistic parameters related to the QRydDemo platform are fixed and realistic effects are reproduced as the decay out of the Rydberg state and a finite temperature for the trapping. The time evolution is performed by exploiting the library QuTiP [48] and

the Bell state fidelity, average gate fidelity, and diamond error rate are returned as output to quantify the quality of the gate. In Chapter 5, we will use this software to investigate which kind of protocol is more suitable for realizing a high-fidelity gate for the QRydDemo platform.

4.3.1 Realistic effects

Imperfect Rydberg blockade

In the program, finite blockade interactions can be accounted for. Indeed, a perfect blockade regime is not always a good assumption to work with, since it is possible that the Rydberg blockade condition is not totally satisfied.

Finite lifetime of $|r\rangle$

In the program, the decay out of the Rydberg state $|r\rangle$ toward a generic state $|d\rangle$ can be taken into account. For simplicity, the state $|d\rangle$ is assumed to be not coupled to the system, i.e. the probability is lost since $|d\rangle$ is not in the computational basis. The collapse operator is defined as:

$$\hat{\mathrm{C}} = \sqrt{\gamma_e}\Big(|d\rangle\langle r| \otimes \mathbb{1} + \mathbb{1} \otimes |d\rangle\langle r| \Big) \tag{4.12}$$

where $\gamma_e = 1/T_r$ is the *decay rate* with t_r the *lifetime* of the state $|r\rangle$.

Finite temperature

The trapping at a finite temperature is simulated with the METTS method [29] illustrated in Sec. 1.6. In particular, for each of the axial and transverse trapping directions, we implement the following thermalizer

$$e^{-\beta\hat{\mathrm{H}}/2} = \exp\left(-\frac{\omega h}{2\beta}\left(\hat{a}^\dagger\hat{a} + \frac{1}{2}\right)\right) \tag{4.13}$$

where $\hat{\mathrm{H}} = 2\pi\omega(\hat{a}^\dagger\hat{a} + \frac{1}{2})$ is the harmonic oscillator Hamiltonian, $\beta = 1/(k_B T)$ with the trapping temperature T and $k_B = 1.38 \times 10^{-23}\,\mathrm{J}\cdot\mathrm{K}^{-1}$, i.e., the *Boltzmann constant*. The number of considered *quantum trajectories* is n_{qt} while the number of METTS that are initially discarded is n_M.

Parameter	Value	Units
Number of oscillator levels $\{n_{ax}, n_{ta_1}, n_{ta_2}\}$	$\{5, 5, 1\}$	–
Trap frequency $\{\omega_{ax}, \omega_{tr}, \omega_{ts}\}$	$\{0.05, 0.3, 0.3\}$	MHz
Trap temperature $\{T_{ax}, T_{tr}, T_{ts}\}$	$\{1, 9, 9\}$	μK
Relative polarizability $\{\alpha_0, \alpha_1, \alpha_r\}$ of $\|0\rangle$, $\|1\rangle$, $\|r\rangle$	$\{1, 1, 1\}$	–
Atom mass m	1.4597×10^{-25}	kg
Lifetime t_r of $\|r\rangle$	50	μs
Wavelength λ_{1r} of the transition from $\|1\rangle$ to $\|r\rangle$	0.323	μm
Waist w_0 of the driving lasers	0.8	μm
C_6 coefficient	-164110	MHz $\cdot$ μm^6
Interatomic distance R	3	μm
Number of considered quantum trajectories n_{qt}	10	–
Generated METTS initially discarded n_M	10	–

TABLE 4.1 • Fixed realistic parameters for two-qubit CZ gate simulation.

Parameters

The realistic parameters in the numerical simulation are fixed as in Tab. 4.1, unless stated differently.

4.3.2 Time evolution

The system's dynamical evolution is computed exploiting the *mesolve* function provided by QuTiP. It is a time-evolution solver for the Lindblad Master equation capable of handling time-dependent Hamiltonians and collapse terms [48]. It takes in input:

- → the system Hamiltonian $\hat{H}_{\text{tot}}$ as in Eq. (4.3);
- → the state at the beginning of the evolution ρ_0;
- → the total time of the evolution and its discretization;
- → if the decay is included, the collapse operator $\hat{C}$ as in Eq. (4.12).

The result is an array with the system evolution vector at each time step. It is projected to the states $|0\rangle$ and $|1\rangle$ to obtain the final state.

We pointed out that the computation can become really intensive if a great number of oscillator levels is considered, since the Hilbert space grows accordingly as we have seen. A way to partially overcome the problem is to *neglect jumps* and use an *effective* Hamiltonian only. The collapse operator in this case is a term added to

the total Hamiltonian $\hat{H}$ as:

$$\hat{H}_{jn} = \hat{H}_{tot} - \frac{i\hat{C}^{\dagger}\hat{C}}{2} \tag{4.14}$$

4.3.3 Extract fidelities

After the dynamical time evolution of the Hamiltonian, the quality of the simulated two-qubit CZ gate is quantified. In the numerical simulation, the following measures are given in output: the average gate fidelity, the diamond error rate and the Bell-state fidelity. The first two measures are briefly discussed in Sec. 1.5. The Bell-state fidelity quantifies the fidelity of the CZ gate by calculating the fidelity of the Bell state $|\Phi^{+}\rangle = (|00\rangle + |11\rangle)/\sqrt{2}$ which can be prepared by a perfect gate operation as discussed in Subsec. 1.2.1. Except for the Bell-state fidelity, the other two measures require quantum tomography in order to be computed.

Chapter 5

CZ Gate Protocols

"The science of today is the technology of tomorrow."

— Edward Teller

In this Chapter, the numerical simulation described in detail in Sec. 4.3 is applied to study the behavior of a two-qubit CZ gate. The aim is to investigate which kind of protocol is more suitable for realizing a high-fidelity gate for the QRydDemo platform. In general, it turns out that the gate is very flexible, in the sense that there are several ways to implement it with numerical high-fidelity.

In Sec. 5.1, we reproduce the protocol of Ref. [17] which consists of two laser pulses of the same length τ with constant Rabi frequency Ω and detuning Δ, but with a phase jump ξ in between. The maximum average gate fidelity obtained is $F_{\text{ave}} = 99.90\%$. Given the drop in performance when a realistic raise time of $40\,\text{ns}$ is introduced on Ω, Δ and ξ, we want to investigate if a time-dependence on the detuning could lead to fidelity improvements both in the case with or without a finite bandwidth. For this purpose, the optimal control algorithm dCRAB is exploited to find the optimal pulse $\Delta(t)$ and parameter ξ which maximize the average gate fidelity. The symmetry of the protocol is mantained, since the detuning of the second pulse is supposed to be the time-reversed of the first one. The minimum pulse duration τ, which still results in a high gate fidelity, is found. For this analysis, we use the open-source version of dCRAB, see Sec. 3.2. We find that the optimal control solution allows to reduce the gate time and it increases also the maximum gate fidelity of $\sim 0.01\%$.

Then, in Sec. 5.2 a protocol with a detuning with a triangular shape, and without phase changes between the two pulses, is implemented. Its performance is really good even under experimental limitations. Also in this case, we use optimal control to further optimize the gate, but we did not obtain improvements both in time nor in fidelity.

Finally, in Sec. 5.3 we show that a protocol with a time-dependent phase $\xi(t)$ and a constant detuning Δ can be transferred into a protocol without a phase change and a time-dependent detuning $\Delta(t)$ by a unitary transformation.

5.1 Constant pulses with phase jump

In this section, we describe the protocol of Ref. [17] and then we recalculate the optimal parameters which realize a gate with high fidelity. After that, we use the optimal control algorithm dCRAB to reduce the duration of the gate and to further increase its performance.

5.1.1 Description

Let us consider the total Hamiltonian, Eq. (4.3), of two neutral atoms in the quantum register. The protocol developed in Ref. [17] consists of two consecutive laser pulses of the same length τ, with detuning Δ and with Rabi frequency Ω. The laser phase of the second pulse is shifted by ξ, namely $\Omega \rightarrow e^{i\xi}\Omega$. In the most simple scenario, we can describe the physics of the system just considering the driving field and the Rydberg blockade mechanism, thus neglecting realistic effects as decay. Then, the system dynamics can be described as:

- the state $|00\rangle$ does not evolve since it is uncoupled by the laser field;
- if one of the two atoms is in the ground state $|0\rangle$, only the system in the excited state $|1\rangle$ evolves. The dynamics can be described with a two-level system with states $|1\rangle$ and $|r\rangle$;
- under a *perfect* Rydberg blockade assumption, if both atoms are initially in $|1\rangle$, the dynamics can be described with a two-level system with states $|11\rangle$ and $\frac{1}{\sqrt{2}}(|1r\rangle + |r1\rangle)$. If an *imperfect* blockade regime holds, a three-level system should be considered where the third state is $|rr\rangle$ as discussed in Subsec. 2.2.1 and Subsec. 4.2.2.

The two-qubit CZ gate (up to a global rotation ϕ of the state $|1\rangle$) is realized by setting Ω, ξ and Δ in such a way that the computational basis states evolve as follows:

$$\begin{aligned} |00\rangle &\rightarrow |00\rangle \\ |01\rangle &\rightarrow |01\rangle\, e^{i\phi} \\ |10\rangle &\rightarrow |10\rangle\, e^{i\phi} \\ |11\rangle &\rightarrow |11\rangle\, e^{i(2\phi-\pi)}. \end{aligned} \tag{5.1}$$

The evolution dynamics on the Bloch sphere of states $|01\rangle$ and $|11\rangle$ is shown in Fig. 5.1. Note that to produce these plots with the numerical simulation, we switch off the traps to have a Hilbert space of dimension 9, namely we set $\{n_{ax}, n_{ta_1}, n_{ta_2}\} = \{1, 1, 1\}$. If all numbers of oscillator levels are set to one, the basis states is given by the tensor product of the basis states of each atom which are $|0\rangle$, $|1\rangle$ and $|r\rangle$. We consider separately the evolution with $|01\rangle$ and $|11\rangle$ as initial states. As discussed, for both of the initial states, the dynamics can be simplified as the one of a two-level system. Thus, to make the plots on the Bloch sphere, we select the states $\{|01\rangle, |0r\rangle\}$ if the system is initially in $|01\rangle$ and $\{|11\rangle, \frac{1}{\sqrt{2}}(|1r\rangle + |r1\rangle)\}$ if it is in $|11\rangle$.

As one can see in Fig. 5.1, the first laser pulse, represented in blue, drives an incomplete oscillation on $|01\rangle$, while the state $|11\rangle$ completes a full cycle of a detuned Rabi oscillation. The second laser pulse, in red, completes the oscillation for a $|01\rangle$ system returning to $|01\rangle$ thanks to the rotation by an angle ξ of its driving field. It also drives a second complete oscillation, around another axis, on the $|11\rangle$ configuration. These plots are valid both in a perfect and imperfect blockade regime, with the exception that in an imperfect blockade case there is also a dynamic toward the state $|rr\rangle$.

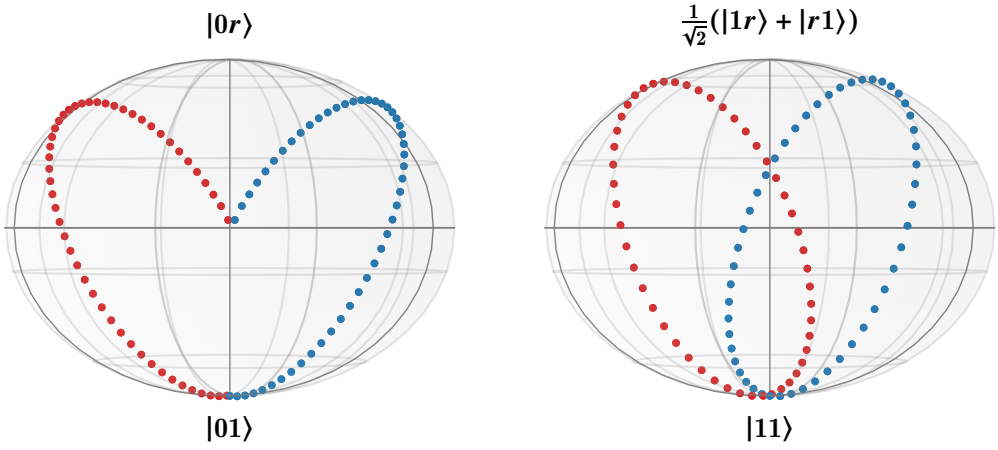

FIGURE 5.1 • Illustration of the dynamic of $|01\rangle$ and $|11\rangle$ states on the Bloch sphere for the protocol with two constant pulses with a phase jump. The initial rotation axis is fixed by the constant detuning; the phase jump has the effect of changing the rotation axis between the two pulses. For a fixed Rabi frequency Ω, optimal detuning Δ and pulse length τ, the first laser pulse (in blue) drives an incomplete Rabi oscillation on the $|01\rangle$ system (see left plot), while the $|11\rangle$ system (see right plot) undergoes a complete detuned Rabi cycle. The phase ξ of the second pulse (in red) is chosen such that for the $|01\rangle$ system the second pulse of length τ completes the oscillation and returns to the state $|01\rangle$. Instead, for the $|11\rangle$ state the second pulse drives a second complete cycle around another axis. See Ref. [17].

5.1.2 Find optimal pulses

The realistic parameters for the numerical simulation of the behavior of the two-qubit CZ gate are fixed as given in Tab. 4.1 and the selected Rabi frequency is $\Omega = 10\,\text{MHz}$. The effects taken into account are: an imperfect Rydberg blockade, decay out of the Rydberg state $|r\rangle$, a Gaussian light beam as well as a finite trapping temperature. The laser misalignment is assumed to be zero. According to the protocol, Ω and Δ are constant with a phase shift ξ between the two pulses. For the beginning, we also neglect that the bandwidth of changing experimental parameters is finite.

The duration of the pulse τ, the detuning Δ, and the phase ξ are determined to minimize the average gate infidelity. To do that, we first fix the pulse duration and for each value of τ we find the optimal Δ and ξ using the `optimize.minimize` function inside the SciPy library [49]. It uses the direct search method of Nelder-Mead for finding the minimum of the objective function [50]. In the end, we select as optimal τ the one with the minimum average gate infidelity with its corresponding optimal Δ and ξ. The best solution found is illustrated in Tab. 5.1. On the left, the optimal values of the parameters are given, while on the right the corresponding average gate fidelity, Bell-state fidelity and diamond error rate are reported. As one can see, the optimal values for the pulses are different with respect to Ref. [17]. This is because we are taking into account finite blockade interactions and the realistic parameters fixed for the simulation are specific of the QRydDemo platform. The fidelities values found for this protocol are high: $F_{\text{ave}} = 99.90\%$ and $F_{\text{b}} = 99.88\%$.

Now, let us briefly analyze the contribution of the different effects on the gate fidelity. If we switch off the effect of the *traps*, namely we set $\{n_{ax}, n_{ta_1}, n_{ta_2}\} = \{1, 1, 1\}$, both the average and the Bell-state fidelity increase by 0.01%. Thus, the trap contribution to the infidelity is really small. The effects of the Gaussian beam are even lower. Instead, if we switch off the *decay* out of the Rydberg state, the average fidelity increases by 0.08%, while the Bell-state fidelity by 0.11%. Thus, the decay effect is the most relevant one and represents a physical limit for the target maximum gate fidelity one can reach with this protocol.

Parameter	Value	Unit	Measurement	(%)
Pulse duration τ	0.0688	μs	Average gate fidelity	99.90
Detuning Δ	3.66	MHz	Bell-state fidelity	99.88
Phase jump ξ	3.87	rad	Diamond error rate	0.434

Table 5.1 • Optimal parameters and fidelity results for the protocol with perfectly constant pulses with a phase jump in the middle. The Rabi frequency is fixed to $\Omega = 10\,\text{MHz}$.

Realistic bandwidth

The assumption of perfectly constant pulses does not hold in the real experiment where one has to consider a finite bandwidth, given for istance by the time to turn on and turn off the laser. In the following, an analysis similar to the previous one is performed. However, the pulses are not anymore assumed perfectly constant but a finite raise time is taken into account. The variables Ω, Δ and ξ are modeled as hyperbolic functions

$$\Omega(t) = \frac{\Omega_{\max}}{2}\tanh\left(\frac{t-\frac{2}{3}t_{\text{rise}}}{a}\right) - \frac{\Omega_{\max}}{2}\tanh\left(\frac{t-2\tau+\frac{2}{3}t_{\text{rise}}}{a}\right) \tag{5.2a}$$

$$\Delta(t) = \frac{\Delta_{\max}}{2}\tanh\left(\frac{t-\frac{2}{3}t_{\text{rise}}}{a}\right) - \frac{\Delta_{\max}}{2}\tanh\left(\frac{t-2\tau+\frac{2}{3}t_{\text{rise}}}{a}\right) \tag{5.2b}$$

$$\xi(t) = \frac{\xi_{\max}}{2}\tanh\left(\frac{x-\tau}{b}\right) + \frac{\xi_{\max}}{2}. \tag{5.2c}$$

For this analysis, we set $a = 0.005$, $b = 0.008$ and the raise time equal to $t_{\text{raise}} = 40\,\text{ns}$. As before, we set $\Omega_{\max} = 10\,\text{MHz}$ and for a fixed τ, the algorithm finds the best $\Delta_{\max}$ and $\xi_{\max}$ in order to minimize the average gate infidelity. Then, the pulse duration τ with the minimum infidelity is chosen as optimal value with its corresponding $\Delta_{\max}$ and $\xi_{\max}$. The best solution is reported in Tab. 5.2 and the corresponding pulse shapes are shown in Fig. 5.2. In this case, the best fidelity $F_{\text{ave}} = 96.65\%$ is dramatically lower with respect to the perfect pulses scenario and the price to pay is also a greater pulse duration $\tau = 120.2\,\text{ns}$. Indeed, more time is needed because with a finite bandwidth on the Rabi frequency Ω less energy is given to the system. However, this is not the main source of infidelity since the time spent in the Rydberg state is not drastically increased. Indeed, if we switch off the decay, the average gate fidelity increase by 0.10% and the Bell-state fidelity by 0.12%. These results are consistent with before. Also the bandwidth in the detuning does not play a major role, since even by removing it the result in fidelity is the same. This leads us to think that the decreasing fidelity is especially a fault of the non-instantaneous phase jump. The conclusion is that this protocol does not work properly anymore when a finite and realistic raise time is considered.

Parameter	Value	Unit	Measurement	(%)
Pulse duration τ	0.1202	μs	Average gate fidelity	98.65
Detuning $\Delta_{\max}$	2.35	MHz	Bell-state fidelity	98.31
Phase jump $\xi_{\max}$	2.31	rad	Diamond error rate	1.422

TABLE 5.2 • Optimal parameters and fidelity results for the protocol with constant pulses with a phase jump in the middle, under the assumption of pulses with a finite bandwidth of $t_{\text{raise}} = 40\,\text{ns}$. The pulse shape is as in Eq. (5.2). We set $a = 0.005$, $b = 0.008$ and $\Omega_{\max} = 10\,\text{MHz}$.

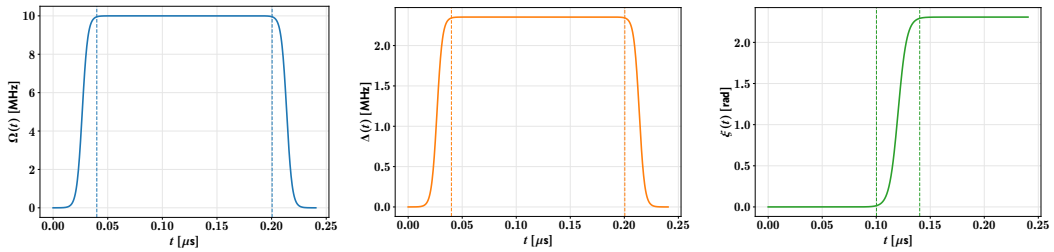

(A) Rabi frequency Ω **(B)** Detuning Δ **(C)** Phase ξ

FIGURE 5.2 • Optimal pulses illustration for the protocol with constant pulses with a phase jump, under the assumption of a finite bandwidth of $t_{\text{raise}} = 40\,\text{ns}$. The pulse shape is as in Eq. (5.2) where we fix $a = 0.005$ and $b = 0.008$.

5.1.3 Optimal control optimization

Now, let us introduce a time-dependent detuning $\Delta(t)$ to investigate if this can improve the performance of the gate. We assume that the two pulses of duration τ are still *symmetric*, namely the detuning shape of the second pulse is the time-reversed of the first one. The realistic parameters for the simulation are again fixed as in Tab. 4.1. Also in this case the effects taken into account are: an imperfect Rydberg blockade, decay out of the state $|r\rangle$, a Gaussian light beam as well as a finite trapping temperature.

Reduce pulse duration

Let us set the Rabi frequency to $\Omega = 10\,\text{MHz}$. We search for the optimal pulse $\Delta(t)$ and constant phase jump ξ in order to find the minimum pulse duration τ which still results in a high gate fidelity, in accordance with the quantum speed limit. The $\Delta(t)$ is optimized through the optimal control algorithm dCRAB, described in Chapter 3. In the following, we suppose that the pulse can be expanded as a truncated Fourier basis with $N_c = 4$ basis functions. The random frequencies follow a uniform distribution between $\omega_{\text{min}} = 0$ and $\omega_{\text{max}} = 3\pi/\tau$ and we assume that the amplitude of the pulse is constrained in the range $[-12 : 12]\text{MHz}$. These limits are chosen in such a way that they fit with the assumed raise time. The initial pulse guess is constant.

To do the optimization, we first fix the pulse duration and for each value of τ we find the optimal pulse $\Delta(t)$ and parameter ξ using the open-source of dCRAB introduced in Sec. 3.2. As before, once the detuning of the first pulse is optimized, the one of the second pulse is just the time-reversed of the first one. The figure of merit to minimize is the average gate infidelity $1 - F_{\text{ave}}$. The number of superiterations is $N_s = 3$, while the number of iteration for each of them is $N = 500$. Since different local minima exist, different optimizations with the same τ and initial guesses can result in slightly distinct fidelities given the randomity nature of

the dCRAB algorithm. Thus, to have statistically meaningful results and to avoid fluctuations on the plots, for each τ the procedure is repeated 10 times. The average of the minimum infidelity achievable is illustrated in Fig. 5.3 for different pulse durations.

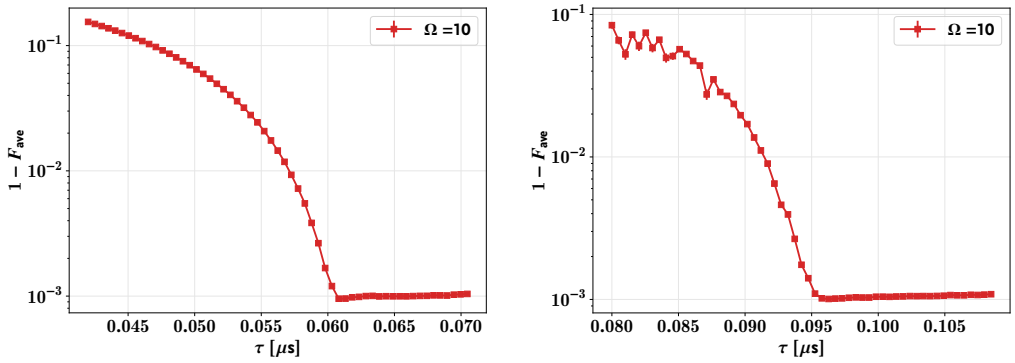

(A) Perfect Ω and ξ **(B)** Finite bandwidth on Ω and ξ

FIGURE 5.3 • Average gate infidelity as a function of the pulse duration τ for $\Omega = 10$ MHz. These plots are obtained by performing an optimization through the dCRAB algorithm: for each τ, the optimal detuning $\Delta(t)$ and the phase parameter ξ are found in order to minimize the average gate infidelity. In **(A)**, the Rabi frequency is assumed to be perfectly constant and the phase jump instantaneous, while in **(B)** a finite bandwidth on Ω and ξ is taken into account. Each point is an average of 10 repetitions.

In particular, Fig. 5.3A refers to the case of perfectly constant Ω and instantaneous phase jump ξ. In this case, one can note that by using optimal control we are able to reduce the pulse duration from ~ 69 ns up to ~ 61 ns. The reduction by approximately 10% in time leads to an increasing of 0.01% of the maximum gate fidelity obtained previously: the best solution is for $\tau = 60.8$ ns with an average gate fidelity $F_{\text{ave}} = 99.91\%$ and a Bell state fidelity $F_{\text{b}} = 99.89\%$. The gain can be interpreted in the following way: a shorter gate time reduces the time spent in the Rydberg state, which is the main source of infidelity. As imposed by the QSL, for the applied parameters it is not possible to reduce the time further since we have a limited pulse power of $\Omega = 10$ MHz. As an example, in Fig. 5.4 we illustrate an optimal detuning pulse found for an optimization with $\tau = 60.8$ ns. As imposed, the detuning is symmetric: the second pulse is the time-reversed of the first one. The related optimized phase jump is $\xi \sim 5.8$ rad. The dynamic on the Bloch sphere for this pulse is illustrated in Fig. 5.5. One can note that with respect to Fig. 5.1, after the first pulse, both $|01\rangle$ and $|11\rangle$ do not complete an oscillation. With the second pulse the two states return to themselves with a different acquired phase.

In Fig. 5.3B, we show the same plot for the case in which a realistic bandwidth is considered for the Rabi frequency and for the phase jump. As in the previous section, Ω and ξ are modeled as hyperbolic functions given by Eq. (5.2a) and Eq. (5.2c), where we set $t_{\text{raise}} = 40$ ns, $a = 0.005$ and $b = 0.008$. We can see that with optimal control we are able to reduce the pulse time from ~ 120 ns to ~ 96 ns.

Not only the gate time can be drastically reduced, but also the maximum gate fidelity achievable now is higher. The best results are $F_{\text{ave}} = 99.90\%$ and $F_{\text{b}} = 99.87\%$ for $\tau = 96.27\,\text{ns}$ in comparison to $F_{\text{ave}} = 98.65\%$ and $F_{\text{b}} = 98.31\%$ for $\tau = 120.2\,\text{ns}$ (see Tab. 5.2).

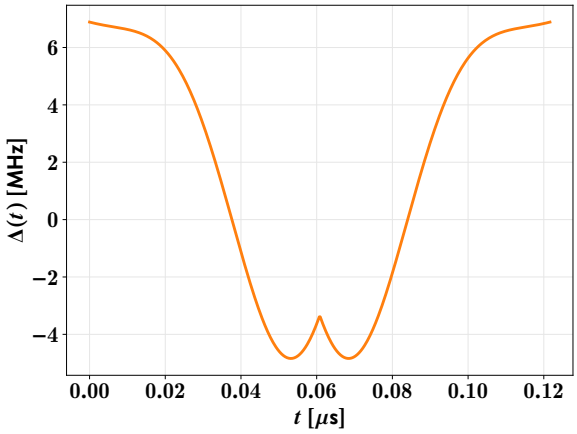

FIGURE 5.4 • Example of optimal $\Delta(t)$ for $\tau = 60.8\,\text{ns}$ found with dCRAB. The total detuning is assumed to be symmetric and once the first pulse is optimized, the second one is the time-reversed. The first pulse is expanded as a truncated Fourier basis with $N_c = 4$ basis functions. The random frequencies follow a uniform distribution between $n_{\text{min}} = 0$ and $n_{\text{max}} = 1.5$ and the amplitude is constrained between $[-12; 12]\,\text{MHz}$. The initial pulse guess is constant.

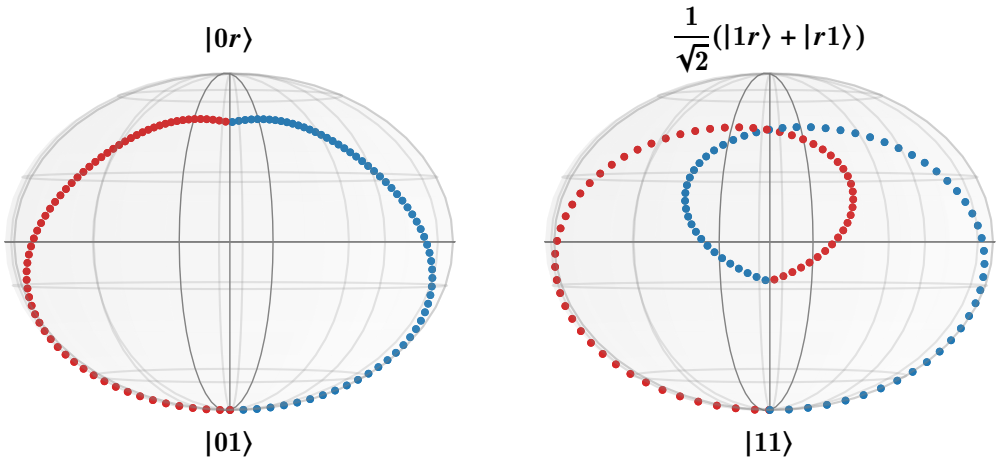

FIGURE 5.5 • Illustration of the dynamic of $|01\rangle$ (left) and $|11\rangle$ (right) states on the Bloch sphere for the protocol with time-dependent detuning as in Fig. 5.4, a phase jump $\xi \sim 5.8\,\text{rad}$ and $\Omega = 10\,\text{MHz}$. The first laser pulse (in blue) drives an incomplete Rabi for both the $|01\rangle$ and $|11\rangle$ states, while the second one (in red) completes the oscillation. The states $|01\rangle$ and $|11\rangle$ returns to themselves with a different acquired phase. Note that, as imposed, the two pulses are symmetric.

Analysis for different Rabi frequencies Ω

As stated previously, shorter gate times reduce the time spent in the Rydberg state. Thus, the contribution of the decay effects, which is the main source of infidelity, can decrease. However, as imposed by the QSL, the minimum gate duration is limited by available resources of the process, as the finite pulse power given by $\Omega = 10\,\text{MHz}$. In this sense, it is interesting to ask how much the gate fidelity improves if more resources are available.

To investigate this curiosity, we fix the Rabi frequency Ω in the range $[10 : 20]$ MHz. For each Ω, the minimum pulse duration τ is found as previously. Thus, we scan a range of different τ and for each one we find the optimal $\Delta(t)$ and ξ which minimize the average gate infidelity. The minimum pulse duration is the one that results in the lower infidelity. In Fig. 5.6A, the result of this analysis is shown. We can see that with a higher Rabi frequency it is actually possible to increase the average gate fidelity: for $\Omega = 20\,\text{MHz}$ and a pulse duration $\tau = 30\,\text{ns}$, we can reach $F_{\text{ave}} \sim 99.95\%$. The minimum pulse durations, related to each infidelity value, are plotted as a function of $1/\Omega$ in Fig. 5.6B. As expected, they are proportional as $\tau = k/\Omega$ and with a linear fit we obtain $k \sim 609\,\text{MHz·s}$. Of course, the pulse duration cannot be reduced close to zero, since for very high Rabi frequencies other physical effects should be taken into account.

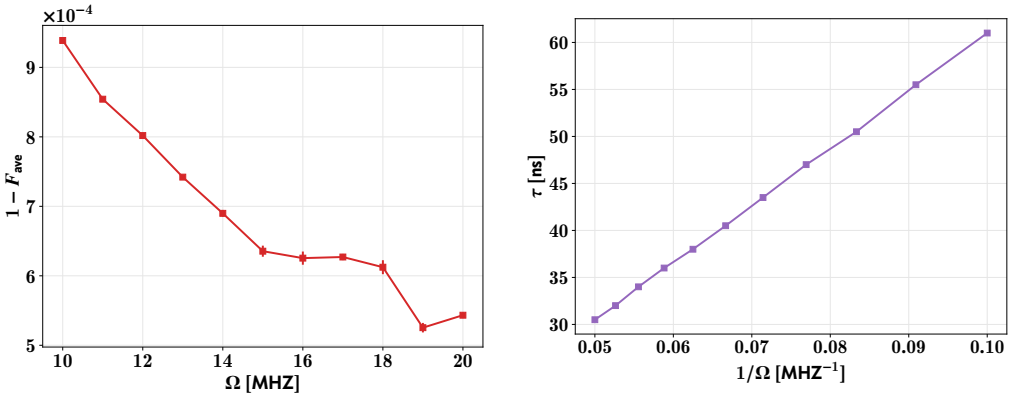

(A) Infidelity vs Ω

(B) τ vs $1/\Omega$

FIGURE 5.6 • In **(A)** a plot of the average gate infidelity as a function of the Rabi frequency is shown. For each Ω, the infidelity value is related to an optimization where τ is the minimum accessible pulse duration in accordance with the QSL. The latter is illustrated in **(B)** as a function of $1/\Omega$. As expected they satisfy a linear relation.

5.2 Time-dependent detuning with triangular shape

In this section, we describe a protocol with a time-dependent detuning (with a triangular shape) and with zero phase. Then we found the optimal parameters which realize a CZ gate with high fidelity. After that, we use the optimal control algorithm dCRAB to investigate if this could lead to an increase in performance.

5.2.1 Description

The optimal control solutions for the detuning look as a triangle and the related phase jumps are really small. Given this intuition, one can ask if a simple protocol with a triangular time-dependence on the detuning and without the phase jump works. Thus, let us slightly modify the previous protocol in the following way. We consider two laser pulses of Rabi frequency Ω and duration τ, but without phase jump in between. This time, the total detuning Δ is time-dependent with a *triangular* shape. The two sides of the triangle have equal length, thus the gate is still symmetric. The map that we want to realize is still given by Eq. (5.1) and the system can be simplified as a two-level system as described previously in Subsec. 5.1.1.

The evolution dynamics on the Bloch sphere of states $|01\rangle$ and $|11\rangle$ is shown in Fig. 5.7. As one can see, for a fixed Ω and a given triangular detuning $\Delta(t)$, the first laser pulse, represented in blue, drives an incomplete oscillation for both the states $|01\rangle$ and $|11\rangle$. This is different with respect to the previous protocol, where the state $|11\rangle$ returns to itself just after the first pulse. The second laser pulse, in red, completes the oscillation making the system initially in $|01\rangle$ or in $|11\rangle$ returning to themselves, but with a different acquired phase. These plots are similar to the ones for the optimal control solution in Fig. 5.5. Indeed, a triangular detuning shape is not so different from the optimal pulses found previously shown in Fig. 5.4. In comparison, now we can note the absence of the phase jump. Indeed, the path on the Bloch sphere is smoother, without any edge between the two pulses.

5.2.2 Find optimal pulses

The realistic simulation of the two-qubit CZ gate is performed with the experimental parameters in Tab. 4.1 and with a Rabi frequency fixed at $\Omega = 10\,\text{MHz}$. As before, the effects taken into account are: an imperfect Rydberg blockade, decay out of the state $|r\rangle$, a Gaussian light beam, a finite trapping temperature and a zero laser

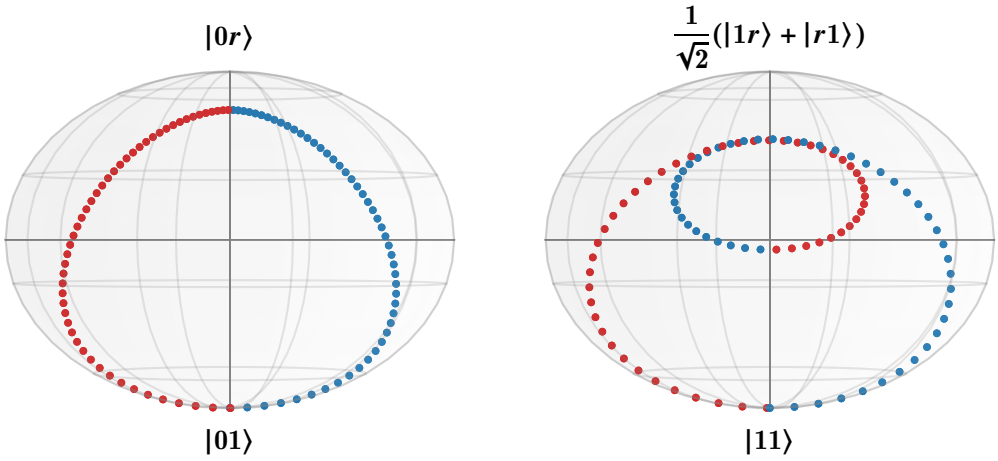

FIGURE 5.7 • Illustration of the dynamic of $|01\rangle$ (left) and $|11\rangle$ (right) states on the Bloch sphere for the protocol with a triangular detuning shape. The initial rotation axis is fixed by the initial detuning, then the axis slightly changes due to the time-dependence $\Delta(t)$. For a fixed Rabi frequency Ω and triangular detuning $\Delta(t)$, the first laser pulse (in blue) drives an incomplete Rabi oscillation for both the $|01\rangle$ and $|11\rangle$ systems. The second pulse (in red) completes the oscillation and returns to the state $|01\rangle$ or $|11\rangle$ with a different acquired phase.

misalignment. According to the protocol, the phase jump ξ between the two pulses is null for the whole gate duration. In the following, Ω is assumed to be perfectly constant, namely no experimental bandwidth is taken into account.

The triangular detuning depends on two free parameters Δ_{max} and Δ_{min}, that represent respectively the maximum and minimum of the equilateral triangle. They are found in order to minimize the average gate infidelity along with the pulse duration τ. The steps of the analysis are the following. Firstly, the pulse duration is fixed and for each value of τ we find the optimal Δ_{max} and Δ_{min} as before, thus using the `optimize.minimize` function. In the end, we select as optimal τ the one with the minimum average gate infidelity with its corresponding optimal parameters. The best solution found is illustrated in Tab. 5.3. On the left, the optimal values of the parameters are given, while on the right the corresponding average gate fidelity, Bell-state fidelity and diamond error rate are reported. The fidelities values found for this protocol are $F_{\text{ave}} = 99.91\%$ and $F_{\text{b}} = 99.89\%$. They are higher with respect to the previous protocol with constant pulses of 0.01% and they reach the values of the ones obtained via dCRAB. Also the optimal pulse duration $\tau = 61.3\,\text{ns}$ is as small as the best optimal control solution. The optimized triangular detuning is plotted in Fig. 5.8. Let us note that the crucial point that seems to make the gate properly working is the change between a positive and a negative detuning with the minimum in the middle. Indeed, a detuning with only negative or positive values results in very low fidelities.

The contributions of the different effects on the gate fidelity are more or less the same as the previous protocol. Thus, by switching off the traps, both the average gate fidelity and the Bell state fidelity increase by 0.01%. If we switch off the decay out of $|r\rangle$, the average gate fidelity increases by $\sim 0.07\%$ and the Bell state fidelity by approximately 0.10%.

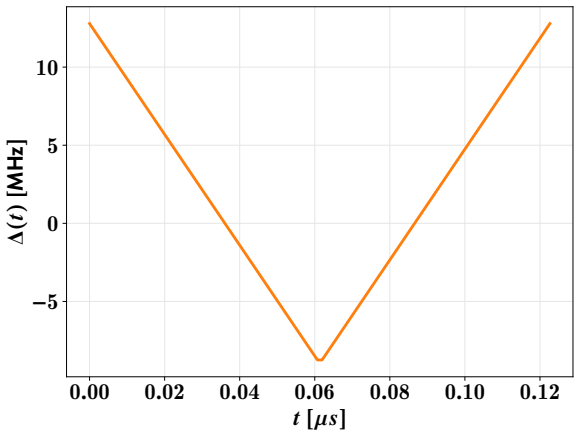

FIGURE 5.8 • Optimal detuning $\Delta(t)$ for the protocol with a triangular detuning shape.

Parameter	Value	Unit	Measurement	(%)
Pulse duration τ	0.0613	μs	Average gate fidelity	99.91
Max detuning Δ_{max}	12.79	MHz	Bell-state fidelity	99.89
Min detuning Δ_{min}	-8.97	MHz	Diamond error rate	0.368

TABLE 5.3 • Optimal parameters and fidelity results for the protocol with a triangular detuning shape under the assumption of a constant Rabi frequency fixed to $\Omega = 10$ MHz.

Realistic bandwidth

Now, let us take into account the experimental limitations. Thus, a finite bandwidth is introduced for the Rabi frequency which is modeled as Eq. (5.2a) with $t_{\text{rise}} = 40$ ns and $a = 0.005$. The $\Delta(t)$ pulse instead is modified in the following way. If $t < t_{\text{rise}}$ or $t > 2\tau - t_{\text{rise}}$, the detuning is assumed to be constant, otherwise it is modeled as a triangle with Δ_{max} and Δ_{min} parameters. However, since a perfect triangular shape is not achievable experimentally, a smoothed function has to be considered. For this purpose, a Savitzky-Golay filter available in SciPy [49] is exploited to slightly smooth the whole Δ array (see Fig. 5.9B). For this analysis, we consider $\Omega = 10$ MHz and for a fixed τ the algorithm finds the best Δ_{max} and Δ_{min} in order to minimize the

average gate infidelity. The pulse duration τ with the minimum infidelity is chosen as optimal value with its corresponding parameters. In Tab. 5.4 we report the best solution, while in Fig. 5.9 the corresponding Ω and Δ pulse shapes are illustrated.

It is really interesting to note that even considering a finite bandwidth for Ω, the maximum gate fidelity is still very high: $F_{\text{ave}} = 99.91\%$ and $F_{\text{b}} = 99.89\%$. Indeed, finite raise time only increases the gate duration up to $\tau = 88.1\,\text{ns}$, since at the beginning we give less power to the system. But, during the raise time the Rydberg state is not populated, thus effects as decay does not affect the gate's performance. In conclusion, in contrast to the previous protocol, this works well also when a finite and realistic raise time is considered, even without using optimal control.

Parameter	Value	Unit	Measurement	(%)
Pulse duration τ	0.0881	μs	Average gate fidelity	99.91
Max detuning Δ_{max}	8.30	MHz	Bell-state fidelity	99.89
Min detuning Δ_{min}	-9.13	MHz	Diamond error rate	0.410

TABLE 5.4 • Optimal parameters and fidelity results for the gate protocol with triangular detuning under the assumption of Ω with a finite bandwidth. Its pulse shape is as in Eq. (5.2), where $t_{\text{raise}} = 40\,\text{ns}$, $a = 0.005$ and $\Omega_{\text{max}} = 10\,\text{MHz}$. The Δ is constant if $t < t_{\text{rise}}$ or $t > 2\tau - t_{\text{rise}}$, otherwise it has a triangular shape. It is also smoothed in order to be experimentally feasible.

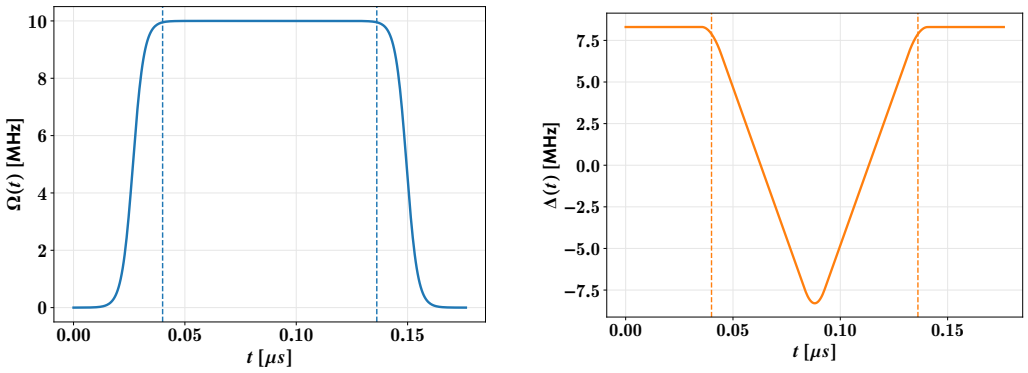

(A) Rabi frequency Ω

(B) Detuning Δ

FIGURE 5.9 • Optimal pulses illustration for the protocol with triangular detuning. The pulse Ω is assumed with a finite bandwidth and its shape is as in Eq. (5.2) where we fix $t_{\text{raise}} = 40\,\text{ns}$ and $a = 0.005$. The Δ is constant if $t < t_{\text{rise}}$ or $t > 2\tau - t_{\text{rise}}$, otherwise it has a triangular shape. It is also smoothed with a Savitzky-Golay filter in order to be experimentally feasible.

5.2.3 Optimal control optimization

Now, let us investigate if it is possible to further reduce the gate time for this protocol by using optimal control. First of all, we fix $\Omega = 10\,\text{MHz}$. In order to find the minimum pulse duration for which a high fidelity is achievable, we scan different values of τ and for each of them the detuning $\Delta(t)$ is optimized through dCRAB. Also in this case, the pulse is expanded as a truncated Fourier basis with $N_c = 4$ basis functions and with uniform random frequencies between $\omega_{\text{min}} = 0$ and $\omega_{\text{max}} = 3\pi/\tau$. The amplitude of Δ is constrained in the range $[-12 : 12]$ MHz and its initial guess is a triangle. As before, we choose $N_s = 3$ and $N = 500$. To have results with a statistic, for each τ the detuning pulse is optimized 10 times.

The minimum average gate infidelity results for the different gate durations are illustrated in Fig. 5.10A. In this case, Ω is assumed to be perfectly constant without any experimental bandwidth. We can note that the best fidelity is again $F_{\text{ave}} \approx 99.91\%$ with the minimum time $\tau \sim 61\,\text{ns}$. Thus, any improvement is possible and the perfectly triangular solution is already the fastest one. Also in the case of a finite bandwidth on Ω, the gate cannot be speeded up nor there are improvements in fidelity as one can deduce from Fig. 5.10B. Here, we have modeled Ω as in Eq. (5.2a) with $t_{\text{raise}} = 40\,\text{ns}$ and $a = 0.005$.

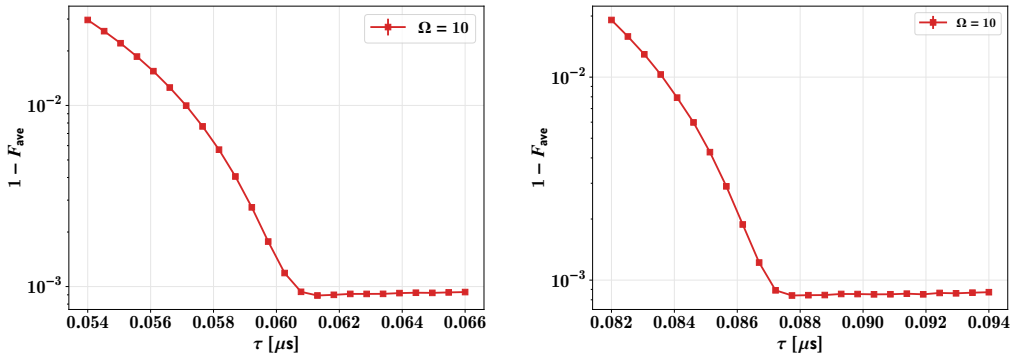

(A) Perfectly constant Ω **(B)** Finite bandwidth on Ω

FIGURE 5.10 • Average gate infidelity as a function of the pulse duration τ for $\Omega = 10\,\text{MHz}$. These plots are obtained by performing an optimization through the dCRAB algorithm: for each τ the optimal pulse $\Delta(t)$ is found in order to minimize the average gate infidelity. The initial guess for the pulse is a triangle and it is expanded as a truncated Fourier basis with $N_c = 4$ basis functions and with uniform random frequencies between $n_{\text{min}} = 0$ and $n_{\text{max}} = 1.5$. Its amplitude is constrained in the interval $[-12 : 12]$ MHz. In **(A)** the Rabi frequency is assumed to be perfectly constant, while in **(B)** a finite bandwidth is considered.

5.3 Relation between the two protocols

As we have seen in the previous sections, there are several ways to implement a two-qubit CZ gate with numerical high-fidelity. We can use a protocol with a constant detuning and a phase jump between the two pulses, but a protocol with only a triangular detuning without any phase jump still works. One can ask if these two protocols are somehow related in a more general framework. To investigate this question, let us consider the atom-light interaction Hamiltonian of one single-qubit, with Rabi frequency Ω, constant detuning Δ and with a time-dependent laser phase $\xi(t)$, given by

$$\hat{\mathrm{H}}_0 = \frac{\Omega}{2} e^{-i\xi(t)} |1\rangle\langle r| + \frac{\Omega^*}{2} e^{i\xi(t)} |r\rangle\langle 1| - \Delta |r\rangle\langle r| . \tag{5.3}$$

We can use the unitary operator

$$\hat{U}(t) = |0\rangle\langle 0| + |1\rangle\langle 1| + e^{i\xi(t)} |r\rangle\langle r| \tag{5.4}$$

to express the single-qubit Hamiltonian in a rotating frame through the transformation defined in Eq. (2.34) [40]. The resulting Hamiltonian is

$$\hat{\mathrm{H}}_{0_{\mathrm{rwf}}} = \frac{\Omega}{2} |1\rangle\langle r| + \frac{\Omega^*}{2} |r\rangle\langle 1| - (\Delta + \dot{\xi}(t)) |r\rangle\langle r| . \tag{5.5}$$

One can note that, in this frame, the oscillating term is removed from the dynamics and the new detuning is given by $\Delta_{\mathrm{rwf}}(t) \equiv \Delta + \dot{\xi}(t)$. The total Hamiltonian of a system of two interacting qubits is

$$\hat{\mathrm{H}} = \hat{\mathrm{H}}_{0_{\mathrm{rwf}}} \otimes \mathbb{1} + \mathbb{1} \otimes \hat{\mathrm{H}}_{0_{\mathrm{rwf}}} - \frac{C_6}{R^6} |rr\rangle\langle rr| . \tag{5.6}$$

If we compare Eq. (5.3) and Eq. (5.5), we can deduce that a protocol with a time-dependent phase $\xi(t)$ and a constant detuning Δ is equivalent to a protocol with a zero phase and a time-dependent detuning $\Delta_{\mathrm{rwf}}(t)$, within a unitary transformation. In the following, let us check if the numerical results are consistent with this relation.

First of all, we fix $\Omega = 10\,\mathrm{MHz}$, Δ is constant for the whole duration of the gate 2τ and we suppose a smooth phase jump defined as the connection of two parabolas

$$\xi(t) = \begin{cases} -bt^2 & t \leq \tau \\ -2b\tau^2 + b(t-2\tau)^2 & \tau < t \leq 2\tau \end{cases} \tag{5.7}$$

where b is an amplitude parameter and τ is the pulse duration. We find Δ and b in order to minimize the average gate infidelity along with the pulse duration τ. As done before, the steps of the analysis are the following. The pulse duration is fixed and for each value of τ we find the optimal Δ and b by using the `optimize.minimize`

Parameter	Value	Unit	Measurement	(%)
Pulse duration τ	0.0613	μs	Average gate fidelity	99.91
Amplitude parameter b	1114	rad/s^2	Bell-state fidelity	99.89
Detuning Δ	12.78	MHz	Diamond error rate	0.365

Table 5.5 • Optimal parameters and fidelity results for a smooth phase jump $\xi(t)$ given by Eq. (5.7) and constant detuning Δ, under the assumption of a constant Rabi frequency fixed to $\Omega = 10$ MHz.

function. In the end, we select as optimal τ the one with the minimum average gate infidelity with its corresponding optimal parameters. The best solution found is reported in Tab. 5.5 and the optimal phase is shown in Fig. 5.11. One can note that the optimal pulse duration $\tau = 61.3$ ns is exactly the same as the triangular protocol solution shown in Tab. 5.3. Also the $\Delta \approx 12.78$ is quite similar to $\Delta_{\max}$ and the results in fidelity are still very high: $F_{\text{ave}} = 99.91\%$ and $F_{\text{b}} = 99.89\%$. The slightly difference between the two solutions is ongly given by numerical random errors.

These results are not so surprising, indeed the derivative of $\xi(t)$, defined as Eq. (5.7), is a triangle

$$\dot{\xi}(t) = \begin{cases} -2bt & t \leq \tau \\ 2b(t-2\tau) & \tau < t \leq 2\tau. \end{cases} \tag{5.8}$$

Thus, by mapping $\xi(t) \to 0$ and $\Delta \to \Delta + \dot{\xi}(t)$[1], we obtain the same optimal solution of the protocol with a triangular detuning shape shown in Fig. 5.8. We can conclude that the two protocols are the same within a unitary transformation, with the unitary operator as in Eq. (5.4). It is interesting to compare the path on the Bloch sphere within the two frames of reference. For this purpose in Fig. 5.12 we illustrate the system dynamics with a smooth phase and constant detuning. In comparison with Fig. 5.7, we can note that the rotation axis, initially fixed by the detuning Δ, changes fast due to the time-dependence on the phase. Thus, the overall dynamic in this case is rapidly rotating.

[1] $\dot{\xi}(t)$ is given in units of frequency not in angulary frequency, namely $\dot{\xi}(t) \to \dot{\xi}(t)/(2\pi)$.

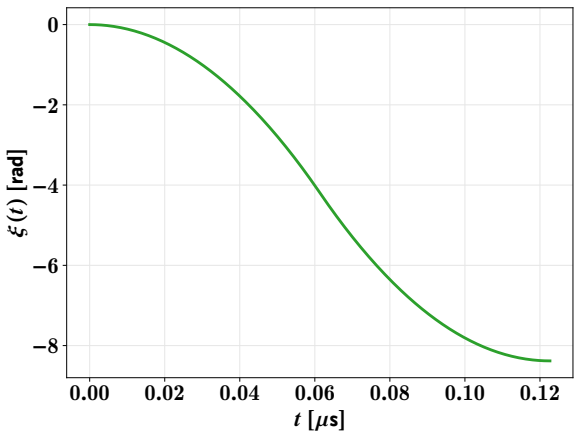

FIGURE 5.11 • Optimal phase $\xi(t)$ with shape as in Eq. (5.7).

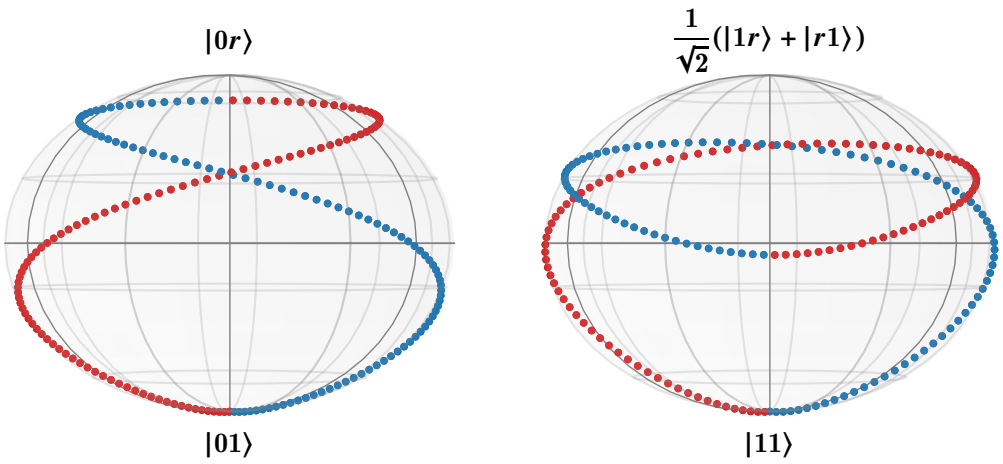

FIGURE 5.12 • Illustration of the dynamic of $|01\rangle$ (left) and $|11\rangle$ (right) states on the Bloch sphere for a time-dependent phase as in Fig. 5.11, a constant detuning $\Delta \sim 12.78\,\text{MHz}$ and $\Omega = 10\,\text{MHz}$. The smoothly changing phase has the effect of changing the rotation axis all the time. The initial rotation axis is fixed by the constant detuning Δ. Also in this case the two pulses, represented in blue and red respectively, are symmetric.

Conclusions and outlook

In this Thesis, we have analyzed in detail the total Hamiltonian of a system of two atoms in a neutral atom quantum register. A numerical simulation of this system has been implemented by Sebastian Weber to reproduce the behavior of a two-qubit controlled-phase gate. Realistic parameters specific for the neutral atom processor developed within the project have been fixed in the simulation. Moreover, realistic effects as imperfect Rydberg blockade, trapping at a finite temperature, and decay out of the Rydberg state have been taken into account. In this work, by using this software, we have benchmarked the gate performance for different protocols through Bell state fidelity, average gate fidelity, and diamond distance measurements.

In a first step, a protocol with a constant detuning Δ and a phase jump ξ is analyzed. In this case, it turns out that the decay out of the Rydberg state is the main source of infidelity, leading to a maximum average gate fidelity achievable of 99.90%. The maximum fidelity reachable is drastically reduced by approximately 1% if a realistic bandwidth for the phase jump ξ, the Rabi frequency Ω and the detuning Δ is taken into account. The infidelity is no more due to the decay effect, as the main source contribution comes from the smoother phase jump. Then, a time-dependent detuning is introduced. To maintain the symmetry of the gate, we set the shape of the second pulse as the time-reversed of the first one. With the optimal control algorithm dCRAB we were able to find an optimal time-dependent detuning $\Delta(t)$ which reduces the pulse duration by approximately 10%, namely from 68 ns to 61 ns. The corresponding average gate fidelity is 99.91%, namely there is an increase of 0.01% since the time that the atoms spend in the Rydberg state is reduced. Also in the case of a realistic bandwidth for the phase jump, the optimal control algorithm allows us to find a solution with a fidelity of 99.91%. The gate time is reduced from 120 ns to 96 ns. Moreover, we performed an analysis of how much we can reduce the gate time if we increase the Rabi frequency Ω.

After that, another protocol for realizing a high fidelity two-qubit CZ gate is discussed. It consists just of a time-dependent detuning with a symmetric triangular shape, thus in comparison with the previous one, the phase jump is neglected. The optimal solution for this case results in an average gate fidelity of 99.91%. The total gate duration is 122 ns. It is already the fastest one, as we have checked by trying to reduce the time by using optimal control techniques.

Finally, we have shown that the protocol with a triangular detuning $\Delta(t)$ and a zero phase is equivalent to the one with a constant detuning Δ and a time-dependent phase $\xi(t)$. They are related by a unitary transformation which expresses the Hamiltonian of the system in a rotating wave frame.

Quantum platforms with trapped neutral atoms in optical tweezers are very promising due to their potential high scalability. Thanks to the recent developments on the control of Rydberg atoms, they offer new opportunities to realize fast two-qubit or multi-qubit gates with high fidelity by exploiting the Rydberg blockade effect. By implementing 2D individually controlled arrays of Strontium-88 atoms and encoding the qubit in two very long-lived states, the main aim of the QRydDemo project is to improve the coherence times of the qubits up to 10 ms, i.e. three orders of magnitude with respect to what demonstrated so far. Different gate schemes will be investigated to figure out which is the best performing one for this platform. The combination of longer coherences times, high-fidelity gates and fast and individual control over each atom in the arrays unlock the possibility for implementing new types of algorithms. In the longer term, it is also fruitful to figure out how many-body gates can help to accelerate quantum circuits. In conclusion, the realization of fully programmable neutral atom devices with hundred of qubits opens many exciting perspectives in quantum computing towards making the quantum advantage a solid reality.

List of Figures

Bibliography

[1] R. P. Feynman, *Simulating physics with computers*, International journal of theoretical physics **21**(6/7), 467 (1982), **doi:**10.1007/BF02650179. (Cited on page ix.)

[2] A. Smith, M. Kim, F. Pollmann and J. Knolle, *Simulating quantum many-body dynamics on a current digital quantum computer* (2019), **doi:**10.1038/s41534-019-0217-0. (Cited on page ix.)

[3] M. C. Bañuls, R. Blatt, J. Catani, A. Celi, J. I. Cirac, M. Dalmonte, L. Fallani, K. Jansen, M. Lewenstein, S. Montangero and et al., *Simulating lattice gauge theories within quantum technologies*, The European Physical Journal D **74**(8) (2020), **doi:**10.1140/epjd/e2020-100571-8. (Cited on page ix.)

[4] A. Ho, J. McClean and S. P. Ong, *The promise and challenges of quantum computing for energy storage*, Joule **2**(5), 810 (2018), **doi:**10.1016/j.joule.2018.04.021. (Cited on page ix.)

[5] J. Preskill, *Quantum computing and the entanglement frontier* (2012), **arXiv:**1203.5813. (Cited on page ix.)

[6] F. Arute, K. Arya, R. Babbush, D. Bacon, J. Bardin, R. Barends, R. Biswas, S. Boixo, F. Brandao, D. Buell, B. Burkett, Y. Chen *et al.*, *Quantum supremacy using a programmable superconducting processor*, Nature **574**, 505–510 (2019). (Cited on page ix.)

[7] A. Montanaro, *Quantum algorithms: an overview*, npj Quantum Information **2**(1) (2016), **doi:**10.1038/npjqi.2015.23. (Cited on page ix.)

[8] M. A. Nielsen and I. L. Chuang, *Quantum Computation and Quantum Information: 10th Anniversary Edition*, Cambridge University Press, **doi:**10.1017/CBO9780511976667 (2010). (Cited on pages ix, 3, and 11.)

[9] J. Preskill, *Quantum computing in the NISQ era and beyond*, Quantum **2**, 79 (2018), **doi:**10.22331/q-2018-08-06-79. (Cited on page ix.)

[10] H.-L. Huang, D. Wu, D. Fan and X. Zhu, *Superconducting quantum computing: A review* (2020), **arXiv:**2006.10433. (Cited on page ix.)

[11] C. D. Bruzewicz, J. Chiaverini, R. McConnell and J. M. Sage, *Trapped-ion quantum computing: Progress and challenges*, Applied Physics Reviews **6**(2), 021314 (2019), **doi:**10.1063/1.5088164. (Cited on page ix.)

[12] L. Henriet, L. Beguin, A. Signoles, T. Lahaye, A. Browaeys, G.-O. Reymond and C. Jurczak, *Quantum computing with neutral atoms*, Quantum **4**, 327 (2020), **doi:**10.22331/q-2020-09-21-327. (Cited on pages ix and 35.)

[13] I. S. Madjarov, J. P. Covey, A. L. Shaw, J. Choi, A. Kale, A. Cooper, H. Pichler, V. Schkolnik, J. R. Williams and M. Endres, *High-fidelity entanglement and detection of alkaline-earth Rydberg atoms*, Nature Physics **16**(8), 857–861 (2020), **doi:**10.1038/s41567-020-0903-z. (Cited on pages ix, x, and 37.)

[14] D. Jaksch, J. I. Cirac, P. Zoller, S. L. Rolston, R. Côté and M. D. Lukin, *Fast Quantum Gates for Neutral Atoms*, Physical Review Letters **85**(10), 2208–2211 (2000), **doi:**10.1103/physrevlett.85.2208. (Cited on page x.)

[15] M. D. Lukin, M. Fleischhauer, R. Cote, L. M. Duan, D. Jaksch, J. I. Cirac and P. Zoller, *Dipole Blockade and Quantum Information Processing in Mesoscopic Atomic Ensembles*, Physical Review Letters **87**(3) (2001), **doi:**10.1103/physrevlett.87.037901. (Cited on page x.)

[16] A. Browaeys and T. Lahaye, *Many-body physics with individually controlled Rydberg atoms*, Nature Physics **16**(2), 132–142 (2020), **doi:**10.1038/s41567-019-0733-z. (Cited on pages x and 21.)

[17] H. Levine, A. Keesling, G. Semeghini, A. Omran, T. T. Wang, S. Ebadi, H. Bernien, M. Greiner, V. Vuleti, H. Pichler and et al., *Parallel implementation of high-fidelity multiqubit gates with neutral atoms*, Physical Review Letters **123**(17) (2019), **doi:**10.1103/physrevlett.123.170503. (Cited on pages x, xi, xii, 47, 48, 49, and 50.)

[18] M. M. Müller, R. S. Said, F. Jelezko, T. Calarco and S. Montangero, *One decade of quantum optimal control in the chopped random basis* (2021), **arXiv:**2104.07687. (Cited on pages xi, 29, and 30.)

[19] Y. B. Band and Y. Avishai, *5 - quantum information*, In Y. B. Band and Y. Avishai, eds., *Quantum Mechanics with Applications to Nanotechnology and Information Science*, pp. 193–258. Academic Press, Amsterdam, ISBN 978-0-444-53786-7, **doi:**https://doi.org/10.1016/B978-0-444-53786-7.00005-8 (2013). (Cited on page 6.)

[20] F. Robicheaux, T. M. Graham and M. Saffman, *Photon-recoil and laser-focusing limits to Rydberg gate fidelity*, Physical Review A **103**(2) (2021), **doi:**10.1103/physreva.103.022424. (Cited on pages 6 and 26.)

[21] D. Manzano, *A short introduction to the Lindblad master equation*, AIP Advances **10**(2), 025106 (2020), **doi:**10.1063/1.5115323. (Cited on pages 8 and 10.)

[22] V. V. Albert, *Lindbladians with multiple steady states: theory and applications* (2018), **arXiv:**1802.00010. (Cited on page 10.)

[23] X. Xu, J. Thingna, C. Guo and D. Poletti, *Many-body open quantum systems beyond lindblad master equations*, Physical Review A **99**(1) (2019), **doi:**10.1103/physreva.99.012106. (Cited on page 10.)

[24] A. Gilchrist, N. K. Langford and M. A. Nielsen, *Distance measures to compare real and ideal quantum processes*, Physical Review A **71**(6) (2005), **doi:**10.1103/physreva.71.062310. (Cited on pages 11, 12, and 13.)

[25] I. L. Chuang and M. A. Nielsen, *Prescription for experimental determination of the dynamics of a quantum black box*, Journal of Modern Optics **44**(11-12), 2455–2467 (1997), **doi:**10.1080/09500349708231894. (Cited on page 11.)

[26] J. B. Altepeter, D. Branning, E. Jeffrey, T. C. Wei, P. G. Kwiat, R. T. Thew, J. L. O'Brien, M. A. Nielsen and A. G. White, *Ancilla-assisted quantum process tomography*, Physical Review Letters **90**(19) (2003), **doi:**10.1103/physrevlett.90.193601. (Cited on page 12.)

[27] M. A. Nielsen, *A simple formula for the average gate fidelity of a quantum dynamical operation*, Physics Letters A **303**(4), 249–252 (2002), **doi:**10.1016/s0375-9601(02)01272-0. (Cited on page 12.)

[28] G. Benenti and G. Strini, *Computing the distance between quantum channels: usefulness of the fano representation*, Journal of Physics B: Atomic, Molecular and Optical Physics **43**(21), 215508 (2010), **doi:**10.1088/0953-4075/43/21/215508. (Cited on page 13.)

[29] E. M. Stoudenmire and S. R. White, *Minimally entangled typical thermal state algorithms*, New Journal of Physics **12**(5), 055026 (2010), **doi:**10.1088/1367-2630/12/5/055026. (Cited on pages 13, 14, and 44.)

[30] S. R. White, *Minimally entangled typical quantum states at finite temperature*, Physical Review Letters **102**(19) (2009), **doi:**10.1103/physrevlett.102.190601. (Cited on page 14.)

[31] D. S. Weiss and M. Saffman, *Quantum computing with neutral atoms*, Physics Today **70**(7), 44 (2017), **doi:**10.1063/PT.3.3626. (Cited on pages 15 and 23.)

[32] T. F. Gallagher, *Rydberg Atoms*, Cambridge Monographs on Atomic, Molecular and Chemical Physics. Cambridge University Press, **doi:**10.1017/CBO9780511524530 (1994). (Cited on pages 16 and 19.)

[33] T. L. Nguyen, *Toward quantum simulation with Rydberg atoms*, Ph.D. thesis (2016). (Cited on pages 16 and 20.)

[34] J. Lim, H.-g. Lee and J. Ahn, *Review of cold rydberg atoms and their applications*, Journal of Korean Physical Society **63**, 867 (2013), **doi:**10.3938/jkps.63.867. (Cited on page 20.)

[35] S. Weber, C. Tresp, H. Menke, A. Urvoy, O. Firstenberg, H. P. Büchler and S. Hofferberth, *Calculation of Rydberg interaction potentials*, Journal of Physics B: Atomic, Molecular and Optical Physics **50**(13), 133001 (2017), **doi:**10.1088/1361-6455/aa743a. (Cited on page 20.)

[36] N. J. Maximilian, *Interacting Rydberg atoms : coherent control at Förster resonances and polar homonuclear molecules*, Ph.D. thesis, **doi:**10.18419/opus-5080 (2012). (Cited on page 21.)

[37] A. M. Kale, *Interacting Rydberg atoms : coherent control at förster resonances and polar homonuclear molecules* (2020), **doi:**10.7907/8mee-md98. (Cited on pages 23 and 41.)

[38] J. Ye, H. J. Kimble and H. Katori, *Quantum state engineering and precision metrology using state-insensitive light traps*, Science **320**(5884), 1734 (2008), **doi:**10.1126/science.1148259, **arXiv:**https://science.sciencemag.org/content/320/5884/1734.full.pdf. (Cited on page 24.)

[39] D. Stuart, *Manipulating single atoms with optical tweezers*, Ph.D. thesis, Oxford University, UK (2014). (Cited on page 24.)

[40] K. Fujii, *Introduction to the rotating wave approximation (rwa) : Two coherent oscillations* (2014), **arXiv:**1301.3585. (Cited on pages 25 and 61.)

[41] J. J. Sakurai and J. Napolitano, *Modern Quantum Mechanics*, Cambridge University Press, 2 edn., **doi:**10.1017/9781108499996 (2017). (Cited on page 25.)

[42] K. Gillen-Christandl, G. D. Gillen, M. J. Piotrowicz and M. Saffman, *Comparison of gaussian and super gaussian laser beams for addressing atomic qubits*, Applied Physics B **122**(5) (2016), **doi:**10.1007/s00340-016-6407-y. (Cited on page 26.)

[43] T. Caneva, T. Calarco and S. Montangero, *Chopped random-basis quantum optimization*, Physical Review A **84**(2) (2011), **doi:**10.1103/physreva.84.022326. (Cited on page 29.)

[44] Y.-Y. Wang and M.-F. Fang, *Quantum speed limit time of a non-hermitian two-level system*, Chinese Physics B **29**(3), 030304 (2020), **doi:**10.1088/1674-1056/ab6c45. (Cited on page 31.)

[45] A. Traverso, R. Chakraborty, Y. Escobar, P. Mickelson, S. Nagel, M. Yan and T. Killian, *Inelastic and elastic collision rates for triplet states of ultracold strontium*, Physical Review A **79**, 060702 (2009), **doi:**10.1103/PhysRevA.79.060702. (Cited on page 36.)

[46] M. Endres, H. Bernien, A. Keesling, H. Levine, E. R. Anschuetz, A. Krajenbrink, C. Senko, V. Vuletic, M. Greiner and M. D. Lukin, *Cold matter assembled atom-by-atom* (2016), **arXiv:**1607.03044. (Cited on page 38.)

[47] J. Bateman, A. Xuereb and T. Freegarde, *Stimulated raman transitions via multiple atomic levels*, Physical Review A **81**(4) (2010), **doi:**10.1103/physreva.81.043808. (Cited on page 39.)

[48] J. Johansson, P. Nation and F. Nori, *Qutip 2: A python framework for the dynamics of open quantum systems*, Computer Physics Communications **184**(4), 1234–1240 (2013), **doi:**10.1016/j.cpc.2012.11.019. (Cited on pages 43 and 45.)

[49] P. Virtanen, R. Gommers, T. E. Oliphant, M. Haberland, T. Reddy, D. Cournapeau, E. Burovski, P. Peterson, W. Weckesser, J. Bright, S. J. van der Walt, M. Brett *et al.*, *SciPy 1.0: Fundamental Algorithms for Scientific Computing in Python*, Nature Methods **17**, 261 (2020), **doi:**10.1038/s41592-019-0686-2. (Cited on pages 50 and 58.)

[50] F. Gao and L. Han, *Implementing the Nelder-Mead simplex algorithm with adaptive parameters*, Computational Optimization and Applications **51**, 259 (2012), **doi:**10.1007/s10589-010-9329-3. (Cited on page 50.)